Diverse Controlling Mechanisms and Teleconnections of Three Distinctive MJO Types

Shihua Liu
Fudan University
Joshua Xiouhua Fu (xfu@hawaii.edu)
IPRC, SOEST, University of Hawaii at Manoa https://orcid.org/0000-0001-5025-0081
Zhiping Wen
Fudan University
Peng Zhang
Fudan University

Research Article

Keywords: Diverse Controlling Mechanisms, Teleconnections, synergetic glocal approach, internal atmospheric processes, nature

Posted Date: November 30th, 2021

DOI: https://doi.org/10.21203/rs.3.rs-1048002/v1

Abstract

In present study, three distinctive MJO types in boreal winter are documented and their controlling mechanisms and teleconnections are investigated with a synergetic glocal approach. For the first time, it is revealed that the diverse nature of the MJO primarily results from different Tropical-Extratropical Interactions and associated internal atmospheric processes. Both the type-I and type-II are initiated over the western Indian Ocean (IO) by a dry zone around the eastern IO, while only the type-I can move out the IO and circulate around the globe. The type-III initiates over the western Pacific (WP) and can circulate the globe and trigger another successive event. The strong upper-level equatorial westerly over the IO-WP, resulting from upstream and extratropical influences, suffocates the type-II MJO within the IO. On the other hand, the robust upper-level equatorial easterly over the IO-WP, also resulting from upstream and extratropical influences, along with regional convective instability over the WP and the arrival of east-Asian cold-surge foster the development and eastward propagation of the type-III MJO. The downstream and extratropical teleconnections are primarily controlled by the associated convection over the tropical IO-WP sector for the type-I, but also strongly influenced by the conditions over the extratropical WP for the type-II and type-III. Given that the MJO has been traditionally viewed as a tropical mode owing its existence to the coupling between organized convection and large-scale circulations, present findings advocate the MJO as a global mode and call for more research on the involved Tropical-Extratropical Interactions in order to better understand and simulate the diverse nature of the MJO.

1. Preface

Under a rapid changing climate (IPCC, 2021), in response to the grand challenges faced by our planet to build a sustainable future, seamless prediction has emerged as a new endeavor for global weather-climate communities (e.g., Hoskins 2013; WMO 2015), which aims to integrate two traditionally separated communities together (i.e., the weather community and climate community). Weather community focused on advancing daily weather forecasting, which is basically an initial condition problem. With more-than-half-century efforts to improve observational platforms and advance data assimilation techniques, and high-resolution modern global/regional atmospheric models, the weather forecasting skill is reaching its theoretical upper limit (~ two weeks) bounded by the stochastic nature of the weather. Climate community focused on advancing seasonal-mean climate prediction, which is largely a boundary condition problem with its predictability primarily originating from land-ocean-sea ice anomalies. Since the successful forecasting of 1987 El Ni o (e.g., Barnett et al. 1988), climate prediction also made great progresses in past decades with the enhanced global observational systems and the advancements of global atmosphere-land-ocean-sea ice coupled models. To bridge the gap between the weather forecasting and climate prediction, global weather-climate communities have been spearheading to improve the understanding of intra-seasonal variability, in particular the Madden-Julian Oscillation (MJO, Madden and Julian 1972, 1971; Lau and Waliser 2012), and to develop Unified weather-climate Forecast Systems (e.g., the NOAA UFS system[1]).

Since the discovery of the MJO (Madden and Julian 1971, 1972), fifty years' synergetic community efforts have led to tremendous progresses in the understanding of major candidate processes governing the MJO (e.g., Lau and Waliser 2012; Maloney and Hartmann 2000; Zhang 2005, 2013; Lin et al. 2009; Zhang et al. 2020). However, present-day global weather and climate models still have numerous problems to simulate and forecast the MJO and its global impacts faithfully (e.g., Hung et al. 2013; Ling et al. 2017). The limited progress made in simulating and forecasting the MJO and its global impacts reflects our lack of comprehensive understanding of the nature of the MJO, partly due to our treatment of the MJO simply as a canonical mode as depicted in Madden-Julian's seminary papers. Theoretical studies aim to capture the essential features of the MJO (e.g., the dominant spatial pattern, period, and propagating speed as reviewed in Zhang et al. 2020). Most modeling studies intend to reproduce the gross features of the MJO (e.g., variance pattern, power spectrum, and regression patterns, Hung et al. 2013). In fact, the MJO represents a quasi-oscillating mode with a broad wavenumber-frequency band (e.g., Roundy 2012), manifesting as a phenomenon with diverse event-by-event variants (e.g., Goulet and Duvel 2000; referred as MJO diversity hereafter).

An emerging challenge faced by the community is to address the following two questions: (1), what are the major processes leading to the diverse nature of the MJO in terms of their onsets, propagations, and teleconnections? and (2), how to faithfully represent these processes in present-day weather and climate models? In literature, the onsets of the MJO over the western Indian Ocean (WIO) might have diverse origins: (i), developing locally, or (ii), being triggered by tropical circumnavigating or extratropical influences. The MJO may develop locally through so-called discharge-recharge processes involving air-sea fluxes (Shinoda et al. 1998; Li et al. 2008; Fu et al. 2017, 2018b), boundary-layer moisture convergence (Wang and Schlesinger 1999; Kemball-Cook and Weare 2001; Chen and Wang 2019) and radiation-convection feedback (Bladé and Hartmann 1993; Qi Hu and Randall 1994; Maloney et al. 2010). Fu et al. (2015) found that some MJO events are strongly coupled to underlying ocean, while others are largely controlled by atmospheric internal dynamics (Harris et al. 2020). A precedent MJO event can also trigger a new MJO over the WIO through its upper-level circumnavigating zonal wind and/or divergence anomalies (Lau and Peng 1987; Hendon 1988; Roundy 2014; Sakaeda and Roundy 2015) and/or low-level Rossby-wave-like response to precedent dry phase around the Maritime Continent (MC, Seo and Kim 2003; Jiang and Li 2005; Zhao et al. 2013). Equatorward-propagating extratropical wave-trains and cold-surges were also observed to trigger the onsets of the MJO (Liebmann and Hartmann 1984; Murakami 1988; Hsu et al. 1990; Ray et al. 2009; Gloeckler and Roundy 2013; Ling et al. 2013, 2014; Zhao et al. 2013; Hong et al. 2017). Matthews (2008) classified all MJO events into two types: primary and successive. The primary MJO is not precedent with another event, while the successive MJO is.

Once initiated, the MJO propagates eastward, but not all of them can move out of the IO (Rui and Wang 1990; Hendon and Salby 1994; Hagos et al. 2016; Kerns and Chen 2016; Ling et al. 2019) . Wang and Rui (1990) first documented the diverse propagating routes of the MJO convection over the MC with daily OLR. Kim et al. (2014) and Feng et al. (2015) found that some MJO events initiated in the IO can't propagate over the MC, while others can. The potential physical processes leading and halting the MJO eastward propagation have been investigated in the contexts of internal atmospheric processes (e.g.,

Wang 1988; Kemball-Cook and Weare 2001; Hsu and Li 2012; Kim et al. 2014; Feng et al. 2015; DeMott et al. 2018) and large-scale environmental conditions (e.g., Waliser et al. 1999; Matthews 2000; Hirata et al. 2013; Roundy 2014; Chen and Wang 2018; Wang et al. 2019). Hirata et al. (2013) and Fu et al. (2018a) discovered that, no matter in boreal winter or summer, the MJO exhibits three distinctive downstream evolutions on its passages over the MC: (i), smoothly transitioning from the IO to WP (type-I); (ii) rapidly decayed over the MC (type-II); and (iii) significantly intensified over the MC (type-III). Coherent positive SST anomalies are found to systematically lead the type-I MJO convection, but not the type-II and type-III. Fu et al. (2018a) further revealed that a robust Sea-Level-Pressure (SLP) tongue as a Kelvin-wave response to the IO MJO convection (Madden and Julian 1972; Matthews 2000) consistently leads the type-I and type-III, but not the type-II. It is found that, for the type-II, a lingering convection over the western North Pacific (WNP) and a severe dry phase over the equatorial WP block the formation of Kelvin-wave response to the east of the convection, thus halting any further eastward propagation of the type-II MJO.

In fact, the type-I and type-II MJOs of Hirata et al. (2013) and Fu et al. (2018a) are very similar to the propagating and non-propagating MJOs defined by Kim et al. (2014), who emphasized the essential role of a robust dry phase around the MC on the propagating MJO. The Rossby-wave response to the dry phase generates a significant positive anomaly of Moist State Energy (MSE) ahead of the IO convection through meridional advection of climatological maximum moisture near the equator. However, Feng et al. (2015) pointed out that the MJO can propagate eastward with or without the suppressed convective phase of OLR, and the positive moisture tendency fundamentally differentiates the propagating and non-propagating MJO events. A recent study of Chen and Wang (2018) supported the importance of a precedent dry phase on the propagating MJO as argued by Kim et al. (2014). They revealed that a robust front walker cell efficiently couples the IO MJO convection with the strong dry phase ahead. This coupling enhances the leading low-level anomalous easterly, boundary-layer convergence (Wang 1988), boundary-layer moisture (Hsu and Li 2012) and convective instability (Kemball-Cook and Weare 2001). Moreover, they further demonstrated two ways from which the suppressed dry phase originates: (i), the preceding dry phase over the IO associated with the previous MJO; (ii), the interaction between the MJO related tropical heating and the corresponding tropical-extratropical teleconnection (Kiladis et al. 2005; Johnson et al. 1999; Zhang 2005; Benedict and Randall 2007).

Taking one step further, we utilized a global-to-local (aka, glocal) approach with multiple perspectives (i.e., A large-scale circulation perspective, a tropical-extratropical interaction perspective, a regional perspective, and a moisture-budget perspective) in this study to investigate the diverse physical processes governing the initiations and propagations of different MJO types. The remaining part of this article is organized as follows. The data and methods used to select different MJO types are given in section 2. The diverse MJO features, the global and local controlling mechanisms as well as the associated teleconnections are detailed in section 3. The last section summarizes our major findings and discusses possible implications and potential pathways forward.

2. Data And Methodology

2.1, Data

The datasets used in this study include the daily-mean Outgoing Longwave Radiation (OLR) with 2.5° 2.5°horizontal resolution from National Oceanic and Atmospheric Administration (NOAA) polar-orbiting satellites (Liebmann and Smith 1996) and the ERA5 [1] hourly data with 0.25° 0.25° horizontal resolution, which have been made available to public as part of the Copernicus Climate Change Service (Hersbach et al. 2018, 2020). The variables from the ERA5 include one-level surface temperature, sea level pressure; and ten-level (from 1000 to 100-hPa) zonal and meridional winds, vertical pressure velocity, geopotential height, air temperature, and specific humidity. To be consistent with the OLR data grid and time interval, the ERA5 data are interpolated onto the 2.5° 2.5° horizontal resolution and accumulated up to daily-mean. All data covers the period from 1985 to 2017.

2.2, Methods

Two steps have been taken to extract the intra-seasonal signals: (1), the time mean and first three harmonics of annual climatological cycle are removed from the raw daily time series; (2), a 20-90-day Lanczos bandpass filtering is applied to the preprocessed time series (Duchon 1979).

To examine the teleconnections of the MJO, the extratropical Rossby wave trains are traced with the horizontal wave activity flux (WAF) as defined by Takaya and Nakamura (2001). The WAF vectors are nearly parallel to the group velocity of the extratropical Rossby waves, which provide a good way to track the extratropical wave propagation. The upper-level WAF is calculated with the 200-hPa intra-seasonal stream function and climatological horizontal winds during the extended winter (NDJFMA).

The boundary-layer moisture budget is assessed with (1000-700-hPa) integrated 20-90-day-filtered moisture tendency equation (Yanai et al. 1973; Hsu and Li 2012). The statistical significance of all composite fields has been tested with the two-sided Student's *t* test (Brown and Hall 1999).

2.3, The Selection of Different MJO Types

The procedure that we used to select different MJO types is largely adopted from Hirata et al. (2013) and DeMott et al. (2018). First, the 20-90-day bandpass-filtered OLR anomaly is averaged between 10°N-10°S for boreal winter (NDJFMA). Then, a simple Empirical Orthogonal Function (EOF) analysis is applied to extract the dominant modes. The first two leading EOF modes explain more than 44.5% of the total variance. They, respectively, represent the MJO cycle with dry peak phase over the IO and the WP (Kessler 2001; Hirata et al. 2013). Third, MJO events are selected and classified into different types based on the principal components (PC1, PC2) of the first two EOFs. For the type-I, a minimum PC1 (day 0 for composite) less than -0.85 standard deviation is followed by a minimum PC2 less than -0.85 standard deviation within 25 days. The type-II only has a minimum PC1 without a minimum follow-up PC2, while the type-III only has a minimum PC2 without a precedent minimum PC1.

For the entire study period (1985-2017), 167 MJO events are selected. Among them, 93 events are classified as type-I, 33 events as type-II, and 41 events as type-III. To ensure the robustness of the events' classification (e.g., Feng et al. 2015; DeMott et al. 2018), the Hovm ller diagrams of the intra-seasonal OLR anomalies averaged over 10°N-10°S of all 167 selected MJO events are further scrutinized with additional criteria. For the type-I, it is required that the contour of -4.5 Wm^{-2} should extend from the IO to WP continuously beyond 125°E with a gap less than 5° longitude. For the type-II, the convection should show continuous eastward-propagation in the IO with at least 30° longitude, but not beyond 125°E (Feng et al. 2015; DeMott et al. 2018). For the type-III, the contour of -4.5 Wm^{-2} starts around the MC and propagates eastward to the WP continuously (Hirata et al. 2013; Fu et al. 2018a). After the second step scrutinization, 114 MJO events are kept with 77, 16, and 21 being the type-I, type-II, and type-III, respectively (The peak dates of all 114 MJO events are given in Table 1 of the supplementary material).

3. Distinctive Factors Shape The Three Mjo Types

3.1, Features of Three MJO Types

Figure 1 gives the composite Hovm ller diagrams of OLR anomalies of three MJO types. For the type-I MJO (Fig. 1a), the convection initiates in the WIO and propagates eastward with intensified amplitude. Upon reaching the MC, the convection is weakened by the topographic blocking (Inness and Slingo 2003; Hsu and Lee 2005; Wu and Hsu 2009; Tan et al. 2020) and strong diurnal cycle over the MC (Sobel et al. 2010; Oh et al. 2012; Hagos et al. 2016). Then, it re-intensifies after crossing the MC to the western Pacific. This propagating characteristics of type-I MJO is consistent to the canonical MJO depicted in many previous studies (Madden and Julian 1972; Lau and Chan 1985; Knutson and Weickmann 1987; Matthews 2000) , or the propagating MJO as classified in some recent literatures (Feng et al. 2015; Kim et al. 2014; Hung and Sui 2018). To the east of the MJO convection, there is a robust eastward-propagating dry phase that was deemed to play a favorable role for the eastward propagation of MJO convection (Kim et al. 2014; Chen and Wang 2018; Wang et al. 2019).

For the type-II MJO (Fig. 1b), a relative weak convection initiates in the WIO and shifts eastward, but rapidly decays before reaching 125 E. The type-II MJO resembles the eastward-decaying events of Hirata et al. (2013) and DeMott et al. (2018). There are two unique features of the type-II MJO: (1), a robust precedent event with convection lingering around the dateline along with the type-II MJO convection over the IO[1]; (2), a severe dry zone persists over the WP. The dry zone over the WP behaves quite differently for the type-I and type-II, which dissipates rapidly in the former case, but not for the latter. To some degree, the severe dry zone in the type-II may be enhanced by the westward-propagating transient dry disturbances, which were also deemed to halt the MJO convection over the IO to propagate into the WP (e.g., Zhu and Wang 1993; Roundy and Frank 2004; Feng et al. 2015; DeMott et al. 2018).

For the type-III MJO (Fig. 1c), the associated convection initiates over the MC instead of the WIO as in the type-I and type-II. The type-III MJO convection, once initiated, rapidly intensifies over the WP and propagates further east to the central Pacific (CP). Unlike the type-I and type-II, no robust dry zone

presents to the east of type-III MJO convection. It is worthy to note that the type-III MJO can not only propagate around the globe but initiate another successive event in the WIO.

The life cycles of the convective signals of three MJO types show distinctive initiation characteristics and downstream evolutions over the MC. There are two favorable MJO initiation places: the WIO for the type-I and type-II; the MC for the type-III. This result is consistent with previous studies (e.g., Kiladis et al. 2014; Hong et al. 2017; Ling et al. 2017). The dry zones to the east of the convection of three MJO types also exhibit distinctive features and potentially impact the MJO evolutions in different ways. More detailed dynamic and thermodynamic processes shaping the initiations and evolutions of three MJO types will be investigated in the following subsections.

3.2, Diverse Controlling Processes of the Three MJO Types

3.2.1, A Large-scale Circulation Perspective

Upper-level velocity potential has long been used to represent the large-scale circulations associated with the MJO (e.g.,Lorenc 1984; Krishnamurti et al. 1985; Knutson and Weickmann 1987). Figs. 2, 3, and 4, respectively, give the composite spatial-temporal life cycles of the 200-hPa velocity potential (hereafter VP200), divergent wind vectors and OLR anomalies for the type-I, type-II, and type-III.

For the type-I MJO from day -25 to -15 (Figs. 2a, b, c), a dry phase develops over the IO, accompanied by the establishment of the upper-level convergent flows (VP200>0). During the same period, a weak convective anomaly along with upper-level divergent flows (VP200<0) in the east of New Guinea dissipates on its way eastward. By day -10 (Fig. 2d), the cross-MC overturning circulation with the descending (ascending) branch over the IO (WP) has evolved into a cross-Pacific overturning circulation with the descending (ascending) branch over the WP (equatorial South America). Together with the arrival of the upper-level divergence, the surface convergence induced by the dry phase over the MC (Zhao et al. 2013) forces a weak convection over the equatorial eastern Africa and the WIO (Fig. 2d).

At day -5 (Fig. 2e), the convection center of the type-I MJO has formed over the WIO with the upper-level divergence sitting around the African-WIO sector. The in-phase relationship between the upper-level divergence and the convection implies that in addition to the low-level forcing, the upper-level divergence also contributes to the development of the convection as suggested by Hendon and Salby (1994), Matthews (2000), and Roundy (2014). At day 0 (Fig. 2f), the MJO convection intensifies rapidly and propagates to the eastern Indian Ocean (EIO). The upper-level divergent center also quickly moves eastward to the EIO co-locating with the convective center. Along with the convective (suppressed) phase over the IO (WP), a regional cross-MC overturning circulation establishes again with the ascending (descending) branch on the western (eastern) side of the MC. During the next two pentads (from day +5 to +10 in Figs. 2g, h), the convection crosses the MC from the IO into WP as well as the upper-level divergence, while the dry zone and upper-level convergence over the WP steadily weaken on their way eastward to tropical South America. A basin-wide cross-Pacific overturning circulation, therefore, is

reestablished with the descending (ascending) branch over the tropical South America (MC). From day +15 to +20 (Figs. 2j, k), the basin-wide cross-Pacific circulation turns into a regional cross-MC circulation along with the formation of a robust dry zone and upper-level convergence over the IO accompanied by the weakening convection and upper-level divergence over the WP.

For the type-II MJO from day -20 to -15 (Figs. 3a, b), a dry zone rapidly forms over the EIO along with the intensified convection over the MC-WP, establishing a regional cross-MC overturning circulation. From day -10 to -5 (Figs. 3c, d), these two anomalous convective signals weaken on their way eastward. At day -5 (Fig. 3d), as the suppressed phase moves to the MC, a weak type-II MJO convection emerges over the WIO. In this case, the convection forms basically due to the surface convergence driven by the dry zone over the MC without any favorable large-scale upper-level divergence. The VP200 anomaly over the IO is still dominated with large-scale convergence: a response to the dry zone over the MC instead of the circumnavigating divergence as in the type-I (Figs. 2d, e). At day 0 (Fig. 3e), the convection anomaly intensifies and slightly extends to the MC. At the same time, the dry zone and upper-level convergence over the WP rapidly amplifies locally rather than propagating eastward to the EP. Thus, unlike the type-I, the basin-wide cross-Pacific overturning circulation is absent in the type-II. Moreover, the strong dry zone and upper-level convergence stay over the MC-WP, together with a lingering convection and upper-level divergence around the dateline from day 0 to +5 (Figs. 3e, f). The strong dry zone over the MC-WP blocks the further eastward propagation of the type-II MJO convection, eventually resulting in its decaying over the IO.

For the type-III MJO from day -15 to -10 (Figs. 4a, b), a northwest-southeast tilting dry zone develops over the MC and moves southeastward to the south of New Guinea. At day -5 (Fig. 4c), the type-III MJO convection emerges over the MC in association with the eastward moving upper-level divergence (Figs. 4a, b, c). At day 0 (Fig. 4d), the convection along with an upper-level divergent center rapidly amplifies locally over the MC-WP. During the next two pentads (from day +5 to +10 in Figs. 4e, f), the convection and the associated upper-level divergence weakens and moves eastward to the American sector, leaving the suppressed phase and the robust upper-level convergent zone over the IO-WP sector. Different from the type-I and type-II, the initiation region of the type-III is over the MC-WP instead of the WIO. Moreover, in terms of the large-scale overturning circulation, the regional cross-MC overturning circulations can be seen at days -10, and +5 (Figs. 4b, e), while the basin-wide cross-Pacific ones exist at days -5, 0, and +10 (Figs. 4c, d, f).

3.2.2, A Tropical-extratropical Interaction Perspective

Many previous studies have shown that the tropical convection associated with the MJO has strong influences on the extratropical circulations through teleconnections (Sardeshmukh and Hoskins 1988; Hoskins and Ambrizzi 1993; Matthews and Kiladis 1999; Matthews et al. 2004; Li et al. 2009). At the same time, extratropical disturbances can also affect the initiation and the evolution of MJO convection in the tropics (Hsu et al. 1990; Chang and Chen 1992; Kemball-Cook and Weare 2001; Ray et al. 2009; Ray and Zhang 2010; Ling et al. 2013; Ray and Li 2013; Zhao et al. 2013; Lee et al. 2019). In this subsection,

the diverse tropical-extratropical interactions of three MJO types are investigated with the 200-hPa stream function (hereafter SF200) and associated wave activity flux (hereafter WAF), as given in Figs. 5, 7, 8.

For the type-I at day -15 and -10 (Figs. 5a, b), a pair of cyclonic [SF200<0 (>0) in NH (SH)[2]]) and anticyclonic gyres [SF200>0 (<0) in NH (SH)] straddling on the equator, respectively, develop on the west and east of a robust dry zone over the EIO-MC. Thesequadrupole cyclonic and anticyclonic gyres are classic Kelvin-Rossby-wave responses to the MJO convection (Gill 1980; Jin and Hoskins 1995; Matthews 2000; Seo and Wang 2010; Seo and Son 2012), leading to robust upper-level equatorial westerly and easterly, respectively, over the IO and WP (Fig. 6a). A Rossby-wave train is established over northern Pacific-American-Atlantic sector with alternative anticyclonic and cyclonic gyres residing over the tropical WP-CP, extratropical North Pacific, eastern Russia-to-Alaska and eastern North America (Figs. 5a, b). The last three “CAC”[3] gyres over the Pacific-North American (PNA) region features a positive PNA pattern. In the Pacific sector, the WAF vectors indicate that extratropical waves propagate both northeastward to Alaska-North America and equatorward to eastern Pacific. In the Atlantic sector, wave propagation is primarily equatorward. Therefore, the upper-level easterly over the equatorial western hemisphere (Fig. 6a) results not just from eastward-propagating equatorial Kelvin-wave, but also the extratropical teleconnections in response to the dry phase over the MC (e.g., Sakaeda and Roundy 2015).

From day -5 to 0 (Figs. 5c, d), in association with the onset of type-I MJO convection over the IO and the dry zone moving to the WP, a new set of quadrupole gyres with reversed signs develops over the IO-WP sector. At day 0 (Fig. 5d), a pair of cyclonic gyres is established over the tropical WP. The previous anticyclonic pairs have moved along the equator to the western hemisphere and merged with the extratropical anticyclones. The robust equatorial easterly associated with the intensified anticyclones in the African-WIO sector provides a favorable downward forcing to the intensification of the convection over the IO. As the convection over the IO further intensifies and moves to the EIO-MC at day +5 (Fig. 5e), the quadrupole Kelvin-Rossby-wave response amplifies too. The associated extratropical teleconnections (Fig. 5e) form a “CACA” wave-train over the WNP, north Pacific, north America and north Atlantic. At day +10 (Fig. 5f), this pattern further evolves into a “CACACA” wave-train with one more “CA” pair extending to northern tropical Atlantic-African sector. During day +5 and +10 (Figs. 5e, f), a negative PNA pattern with the “ACA” wave-train has been established over the northern Pacific-American-Atlantic sector, which is about five days after the robust MJO convection develops in the IO (Fig. 5d). This result is consistent with previous findings (Hsu 1996; Mori and Watanabe 2008; Seo and Son 2012; Tseng et al. 2019; Chen 2021).

For the type-II MJO from day -15 to -10 (Figs. 7a, b), the upper-level quadrupole Kelvin-Rossby-wave response forms over the tropical IO-WP region associated with the eastward-moving convection (dry zone) over the MC (IO) as in the type-I. However, the zonal spans of the anticyclonic pairs over the WP are much smaller than that in the type-I (Fig. 6b and Fig. 7b). Instead of propagating eastward as in the type-I, the anticyclonic pairs over the WP rapidly disappear in next pentad (day -5 in Fig. 7c). During the same period (day -15 to -5 in Figs. 7a, b, c), the cyclonic pairs over the western hemisphere along with the equatorial westerly (Fig. 6b) rapidly move eastward to enhance the cyclonic pairs over the IO. As the dry zone moves to the MC-WP, the type-II MJO convection initiates over the IO with unfavorable upper-level

westerly and convergence (Fig. 3d). At day 0 (Fig. 7d), both the convection over the IO and the dry zone over the MC-WP intensifies, but the upper-level anticyclonic pairs as a Rossby-wave response to the IO convection never manifest as in the type-I. From day -5 to 5 (Figs. 7c, d, e), a quasi-stationary elongated cyclonic gyre presents over the northern WP-CP as one lobe of a Pacific-Japan-like pattern (Kosaka and Nakamura 2006; Wu et al. 2020) and/or a persistent North Pacific pattern (Higgins and Mo 1997). The induced convection over the subtropical WP may help sustain the dry phase over the equatorial WP through a meridional overturning cell. Near the eastern end of this elongated cyclonic gyre, the enhanced equatorward wave activity maintains a lingering convection over the equatorial CP during the entire life cycle of the type-II MJO convection over the IO (Matthews and Kiladis 1999; Moore et al. 2010). The lingering convection over the CP keeps feeding the IO with upper-level westerly (Fig. 6b) and blocking the dry zone over the WP and associated upper-level easterly moving downstream. The lack of upper-level easterly “ventilating” flow and the blocking of enhanced dry zone over the MC-WP lead to the rapid decaying of the type-II MJO convection over the IO (Fig. 7e). During the entire life cycle of the type-II MJO, the extratropical downstream response is largely caused by the quasi-stationary cyclonic gyre over the subtropical WP instead of the tropical convection over the IO-WP. Therefore, a negative PNA-like pattern with “ACA” wave-train (similar as in Fig. 1f of type-I) has presented over the northern Pacific-American-Atlantic sector from day -5 to 5 (Figs. 7c, d, e).

For the type-III MJO from day -15 to -10 (Figs. 8a, b), a weak dry zone over the WP along with its Kelvin-wave-like response (i.e., a pair of anticyclones over the equatorial eastern Pacific) gradually moves eastward. The anticyclone sitting around 20^{o}N in the African-Indian sector is intensified by the equatorward-propagating wave activity in association with the positive NAO pattern (Figs. 8b, c; Lin et al. 2009), thus establishing an apparent equatorial easterly on its southern flank (Fig. 6c). At day -5 (Fig. 8c). The precedent upper-level easterly over the equatorial IO is further intensified (Fig. 6c) by the arrival of the eastward-propagating Kelvin-wave-like anticyclonic pairs, providing an efficient “ventilating” flow for the rapid onset of type-III MJO convection around the MC. In response to this convection, a cyclonic gyre is supposed to form over the WNP as a Gill-type response (Rui and Wang 1990). However, there is an anticyclone over the WNP, which was propagated eastward from eastern China (Figs. 8a, b, c). At day 0 (Fig. 8d), the convection over the MC-WP amplifies rapidly along with the enhanced anticyclones in the WNP and southern IO. The associated equatorial easterly almost covers the entire eastern hemisphere (Fig. 6c). The NH cyclonic response to the convection over the MC-WP is shifted about 40° east of its SH counterpart due to the existence of a quasi-stationary anticyclone over the WNP. Therefore, the upper-level equatorial westerly (Fig. 6c) around the dateline is primarily driven by the SH cyclonic gyre. From day +5 to +10 (Figs. 8e, f), the convection over the WP rapidly weakens on its way eastward. The associated cyclonic pairs and equatorial westerly quickly move into the IO and foster the development of a dry zone, which eventually leads to another MJO cycle (Fig. 1c). In terms of the NH extratropical teleconnections, the situation is very similar as for the type-II. The downstream impacts largely originate from the quasi-stationary anticyclone over the WP-CP, instead of a direct response to the MJO-related convection. During the life cycle of the type-III MJO (Figs. 8c, d, e, f), the anticyclone in the northern extratropical Pacific gradually intensifies and moves to the CP. The associated downstream teleconnections over the northern

Pacific-American-Atlantic sector also evolve from a negative PNA-like pattern (Figs. 8c, d) to a positive one (Figs. 8e, f).

In order to better understand the possible processes leading to the rapid development of the type-III MJO convection over the MC-WP around the day 0 (Fig. 8d), the associated 850-hPa wind and stream function (hereafter SF850) anomalies are examined in Figs. 9 and 10. As early as day -10 (Fig. 9b), there is an apparent, yet weak, equatorial easterly anomaly between 130°E and 180° in the north of Australia, which opposes the prevailing westerly along the equator, favoring the development of lower-level convergence (a hint can be seen in Fig. 11i). This equatorial easterly anomaly is forced by a pair of anticyclones straddling on the equator (Fig. 10b). In association with the “ventilating” upper-level easterly over the equatorial IO (Fig. 8c) and large lower-tropospheric convective instability due to tropospheric drying (Fig. 13i), the type-III MJO convection emerges around the MC at day -5. At day 0 (Figs. 9d, 10d), the convection is rapidly intensified by the northerly in the WNP associated with the arrival of a strong east-Asian cold surge. The arrival of the northerly along the east coast of Asia is accompanied by the build-up of a meridionally-oriented anticyclone at lower troposphere, as manifested by the positive SF850 anomaly spreading from eastern Russia to eastern Asia (from day -5 to 0 in Figs.10c, d). This scenario is consistent with previous findings (e.g., Hsu et al. 1990; Chang and Chen 1992; Pang et al. 2018; Wang et al. 2018) that the cold surge-related northerly favors the initiation, intensification and eastward propagation of the MJO convection over the MC-WP through enhancing the lower-level convergence.

3.2.3, A Regional Perspective

In preceding two subsections, the distinctive large-scale circulations in association with three MJO types have been examined. In present and next subsections, we will zoom into the active convection region over tropical Indo-western Pacific domain (from 30^{o}E to 150^{o}W) to investigate the regional dynamic and thermodynamic processes associated with three MJO types during their initiation and evolution periods. Some previous studies have been devoted to understanding the regional dynamic and thermodynamic processes in association with MJO diversity (Hsu and Li 2012; Zhao et al. 2013; Feng et al. 2015; Chen and Wang 2018; Wang et al. 2019). The potentially important regional processes include the discharge-recharge of convective instability (Blade and Hartmann 1993; Kemball-Cook and Weare 2001), the precedent easterly over the IO contributed by both upstream forcing of Kelvin wave and downstream forcing of Rossby wave (Matthews 2000; Seo and Kim 2003; Zhao et al. 2013), boundary-layer convergence, leading dry phase and front walker cell (Hsu and Li 2012; Hsu et al. 2014; Kim et al. 2014; Feng et al. 2015; Chen and Wang 2018), as well as intra-seasonal SST feedback (Li et al. 2008; Fu et al. 2015, 2017, 2018b). To what degree do these regional processes contribute to the initiations and evolutions of the convection associated with three MJO types? To answer this question, the vertical structures of divergence, moisture, equivalent potential temperature (EPT), apparent heat source and moisture sink anomalies (Q1 and Q2, Yanai et al. 1973) along with the associated circulations for three MJO types have been carefully examined in the following (Figs. 11, 12, 13, and 14).

For the type-I MJO (Figs. 11, 12, 13, 14a-d), the boundary-layer convergence, positive moisture and EPT anomalies appear as early as day -15 in the WIO before the emergence of negative OLR anomaly (Figures not shown). From day -10 to -5 (Figs. 11a, b), this boundary-layer convergence along with the positive moisture (Figs. 12a, b) and positive EPT (Fig. 13a, b) anomalies extend eastward to the EIO and upward to mid-troposphere. The associated convection also evolves from shallow and congestus to deep convection (Figs. 14a, b) with an apparent front walker cell to the east of the convection (Chen and Wang 2018). The higher altitude of maximum Q1 than Q2 (Fig. 14b) suggests that eddy vertical flux convergence contributes significantly to apparent heat source, indicating the MJO convection at a rigorous development stage (Johnson et al. 2015). In next two pentads (day 0 and +5, Figs. 11c, d), the deep convergence zone still resides over the EIO-MC with boundary-layer convergence along with positive moisture (Figs. 12c, d) and positive EPT (Fig. 13c, d) anomalies penetrating to the WP (120°E-160°E) already, thus establishing robust rearward-titling structures of the convergence zone, moisture and EPT. A front (backward) walker cell develops on the east (west) of the convection. The alignment of maximum Q2 and Q1 indicates that the MJO convection has transitioned from dominant convective to stratiform regime (Figs. 14c, d). The systematic positive (Q1-Q2) in the troposphere also suggests that radiative heating potentially plays an important role on sustaining the MJO convection. During the entire life cycle of type-I MJO convection (Figs. 11, 12, 13, 14a-d), the boundary-layer convergence, positive moisture and convective instability consistently lead the convection (negative OLR anomaly). This result testifies that the boundary-layer convergence (Hsu and Li 2012; Chen and Wang 2018; Wang et al. 2019), positive moisture (Lin and Johnson 1996; Raymond and Torres 1998; Hsu and Li 2012) and convective instability (Kemball-Cook and Weare 2001; Zhao et al. 2013; Wang et al. 2019) work in a cooperative way for the development and eastward propagation of the type-I MJO convection.

For the type-II MJO (Figs.11, 12, 13, 14e-h), weak and scattering boundary-layer convergence anomalies begin to appear over the tropical IO as early as day -10 (Fig. 11e) although there is still robust convergence (divergence) anomaly in the upper (lower) troposphere, which is consistent with the overwhelmingly positive VP200 in Fig. 3c. The boundary-layer convergence and the equatorial easterly (Fig. 6b) are likely forced by the dry zone around the MC (Zhao et al. 2013). At the same time, weak positive moisture (Fig. 12e) and EPT (Fig. 13e) anomalies also appear over the IO with robust convective instability (Fig. 13e), but without apparent convection (negative OLR anomaly, Fig. 14e). The robust convective instability (Fig. 13e) is primarily caused by mid-tropospheric drying rather than boundary-layer moistening (Figs. 12e and 13e). In the next pentad (day -5 in Fig. 11f), the low-level anomalous convergence intensifies over the IO and slightly extends upward, so do the positive moisture (Fig. 12f) and EPT (Fig. 13f) along with the onset of deep convection (Fig. 14f). A deep front (shallow backward) walker cell forms on the east (west) of the convection. At the same time, a deep divergence zone along with negative moisture and EPT anomalies develop in the WP (Figs. 11, 12, 13f), in association with the lingering convection near the dateline and quasi-stationary cyclonic gyre over the WNP (Fig. 7c). At day 0, fueled by the robust convective instability (Figs. 13f, g), the convection over the IO is further intensified by the positive feedback between the overturning circulation and the diabatic heating. The robust ascending motion along with positive moisture and EPT anomalies occupies the entire troposphere (Figs. 11, 12,

13g). The MJO convection transitions from dominant convective to stratiform regime (Figs. 14f, g). Different from the type-I MJO, the dry zone over the WP is further intensified (Figs. 12f, g) together with the enhanced convection over the IO instead of weakening (Figs. 12b, c). As the backward walker cell disappears, the front walker cell dominates. The enhanced drying and descending motion over the MC-WP hamper the development of leading boundary-layer convergence and moistening (Figs. 11, 12g). At day +5 (Figs. 11, 12, 13, 14h), the convection over the IO rapidly decays due to the lack of efficient upper-level “ventilating” outflows (Fig. 6b) and leading boundary-layer convergence and moistening as well as the intrusion of severe dry zone over the WP (Feng et al. 2015; DeMott et al. 2018) although there is robust leading convective instability over the MC-WP sector (Figs. 13g, h).

For the type-III MJO (Figs. 11, 12, 13, 14i-l), the initial convergence primarily appears over the WIO in the mid-troposphere (700-300-hPa) accompanied by upper-level divergence at day -10 (Fig. 11i). Weak but significant convergence can also be found in the mid-troposphere (700-500-hPa) around 105°E and near the surface around the MC associated with the low-level easterly (Fig. 9b) induced by the dry zone over the MC-WP. At the same time, weak positive moisture, EPT and negative OLR anomalies (Figs. 12, 13i) scatter over the IO, but without significant diabatic heating (Fig. 14i). Robust convective instability develops over a broad region from the WIO to the dateline (Fig. 13i) with that over the WP primarily due to the mid-tropospheric drying instead of boundary-layer forcing. At day -5 (Figs. 11, 12, 13, 14j), a broad zone of upper-level “ventilating” easterly (Fig. 6c) and divergence (Fig. 11j) is established in association with the rapid eastward extension of a pair of anticyclones (Fig. 8c). These favorable upper-level conditions and strong convective instability foster the rapid development of type-III MJO convection along with robust tropospheric and boundary-layer convergence (Fig. 11j) as well as positive moisture and EPT anomalies (Figs. 12 and 13j) over the IO-MC-WP sector. Contrary to the type-II MJO (Fig. 11f), a deep backward (shallow front) walker cell develops to the west (east) of the convection (Fig. 11j). The convection on the west and east sides of about 135^{o}E are, respectively, dominated by stratiform and convective regimes (Fig. 14j). The robust in-situ convective instability (Fig. 13j), along with the arrival of the east-Asian cold surge (Figs. 9d, 10d, 13k), boosts the rapid intensification of deep convection over the WP at day 0 (Figs. 11, 12, 13k). The corresponding convection also shifts from convective to stratiform regime (Fig. 14k). The persistent positive (Q1-Q2) anomalies at the mature stages (with dominant stratiform rainfall) of the type-I (Figs. 14c, d), type-II (Fig. 14g) and type-III (Fig. 14k) MJO convections testify the important role of radiative heating on sustaining the MJO convection regardless the MJO types. Different from both the type-I and type-II, the type-III MJO has a predominant backward walker cell (Figs. 11j, k, l) instead of a dominant front walker cell (Figs. 11b, c, d and 11f, g), likely due to the lack of a robust deep dry zone preceding the type-III MJO convection (Figs. 12j, k, l). At day +5, the boundary-layer convergence (Fig. 11l), positive moisture (Fig. 12l) and convective instability (Fig. 13l) over the CP steer the type-III MJO convection to further propagate eastward.

3.2.4, A Moisture-budget Perspective

Many previous works have emphasized the essential roles of positive boundary-layer moisture anomaly and positive moisture tendency on leading the eastward propagation of MJO convection (e.g., Kemball-

Cook and Weare 2001; Hsu and Li 2012; DeMott et al. 2014; and Feng et al. 2015). For the type-I and type-III, there are apparent positive boundary-layer anomalies leading the eastward-propagating MJO convection, but not for the type-II (Fig. 13). For different MJO events, the boundary-layer moisture controlling processes can be quite different (Kemball-Cook and Weare 2001; Mei et al. 2015). In this subsection, the major processes governing the boundary-layer moisture tendency for three MJO types are investigated through boundary-layer moisture budget analysis (Figs. 15, 16).

For the type-I (Fig. 15a), the positive boundary-layer moisture tendency leads both the initiation and eastward-propagation of MJO convection. The overall evolution of the moisture tendency resembles the horizontal advection term (Figs. 15a, d). Although the magnitudes of the vertical advection and the moisture sink (Figs. 15b, c) are five times larger than other terms, they almost cancel each other (Fig. 15e). Further decomposition of the horizontal advection term into zonal and meridional advection (Fig. 16a, b, c) shows that, during the initiation phase of the MJO, the positive advection between 30^{O}E-90^{O}E is primarily contributed by zonal advection (Zhao et al. 2013; Hung and Sui 2018). On the other hand, the meridional advection leads to the positive advection over the 110°E-180°, favoring the eastward propagation of the MJO (Kiranmayi and Maloney 2011; Kim et al. 2014; Feng et al. 2015; Wolding and Maloney 2015).

For the type-II MJO (Fig. 15f), the leading positive tendency only exists over the IO region, which is mainly contributed by the horizontal advection (Fig. 15i). The maximum positive tendency around 90°E at day -10 (Fig.15f) is also contributed by the moisture sink term although the negative vertical advection plays an opposite role (Figs. 15g, h, j). As in the type-I, the horizontal moisture advection generates positive boundary-layer moisture tendency before the onset of the type-II convection in the IO and to the east of the convection in the WP (Fig. 15i), which is supposed to favor the initiation of convection and its eastward propagation. However, the strong negative vertical advection induced by the dry zone over the WP (Fig. 15g and Figs. 12f, g, h) exceeds the positive moisture sink and horizontal advection (Figs. 15h, i), thus resulting in near-zero boundary-layer moisture tendency east of 105^{O}E (Fig. 15f). The lack of apparent positive boundary-layer moisture tendency east of the IO convection hinders the eastward propagation of type-II MJO (Feng et al. 2015). Further decomposition shows that meridional advection plays a larger role than the zonal advection on the positive horizontal advection term (Figs. 16d, e, f).

For the type-III MJO (Fig. 15k), there is no obvious positive boundary-layer moisture tendency preceding the onset of convection over the MC (from 90°E to 120°E). The coherent positive moisture tendency over the WP (from 120°E to 170°E) around day -10 may favors the rapid eastward migration of the type-III MJO convection through moistening the boundary layer over the WP (Fig. 12j). This result suggests that the boundary-layer process only plays a minor role on the initiation of type-III MJO convection. It is the upper-level easterly “ventilating” flow (Fig. 6c and Figs. 8c, d; Roundy 2014) and large-scale convective instability induced by mid-tropospheric drying (Fig. 13i; Lavender and Matthews 2009) triggers the onset of type-III MJO convection over the MC. As for the Type-I and Type-II, the positive moisture tendency of the type-III over the 120°E-170°E is basically caused by horizonal advection (Fig. 15n). In fact, the coherent positive anomaly extending from the IO to WP has been generated by horizontal advection preceding the

onset of the convection (Fig. 15n). It is the negative vertical advection and moisture sink (Figs. 15l, m) that oppose the positive horizontal advection, resulting in a near-zero overall tendency over the IO-MC. Further decomposition (Figs. 16g, h, i) shows that meridional (zonal) advection dominates the positive horizontal advection west (east) of 120°E.

4. Concluding Remarks And Discussions

In order to gain an overall insight about the potential roles of the tropical-extratropical interactions, top-down and bottom-up influences along with the tropical internal atmospheric processes on shaping the MJO diversity, a synergetic glocal approach with multiple perspectives has been taken to comprehensively investigate the diverse MJO nature and associated controlling mechanisms and teleconnections. This unique approach enables us to reveal, at the first time, that the diverse nature of the MJO primarily results from the influences of different tropical-extratropical interactions on tropical internal atmospheric processes.

Following previous studies (Hirata et al. 2013; Feng et al. 2015; Fu et al. 2017; DeMott et al. 2018), a set of combined objective and subjective criteria have been applied to obtain three distinctive MJO types (Table 1 of the supplementary material). Both the type-I (Fig. 1a) and type-II MJO (Fig. 1b) initiate over the western IO associated with dry zones on the east. The type-I resembles the canonical MJO depicted in many previous studies (e.g., Madden and Julian 1972; Knutson and Weickmann 1987), which can propagate around the globe. The type-II can’t propagate out of the IO, resembling the non-propagation events in some previous works of literature (e.g., Kim et al. 2014; Feng et al. 2015). In association with the type-II convection over the IO, there is a lingering convection over the CP (Fig. 1b), like the composite of Sakaeda and Roundy (2015) with upper-level westerly wind over western hemisphere (their Fig. 1b). The type-III (Fig. 1c) initiates rapidly over the WP without any robust dry zone associated, which can circulate around the globe and trigger another successive event over the IO.

To investigate the dominant controlling mechanisms and associated teleconnections of three MJO types, a synergetic glocal approach with multiple perspectives has been applied in this study. Major findings from individual perspectives have been summarized in the following.

A Large-scale Circulation Perspective

the global large-scale overturning circulations associated with three MJO types are examined in Figs. 2, 3, 4. As discovered in Fu et al. (2018a) for three boreal-summer MJO types, the life cycle of the type-I MJO is alternatively dominated with basin-wide cross-Pacific overturning circulations (e.g., Figs. 2d, g) and regional cross-MC overturning circulations (Figs. 2b, f, k). The type-II MJO is associated mainly with regional cross-MC overturning circulations (Fig. 3). The type-III MJO, however, is primarily associated with cross-Pacific basin-wide circulations (Fig. 4). The onsets of type-I and type-III MJO convection are preceded by upper-level circumnavigating divergence (Fig. 2d and Fig. 4b), but not for the type-II.

A Tropical-extratropical Interaction Perspective

the global teleconnections and associated tropical-extratropical interactions of three MJO types are evaluated in Figs. 5, 6, 7, 8, 9 and 10. For the type-I (Fig. 5), the extratropical teleconnection and downstream response synchronize well with each other to support the development and eastward propagation of the MJO convection. A robust upper-level easterly anomaly (Figs. 5d, e and Fig. 6a), as a downstream and extratropical response to previous dry phase, provides a favorable condition for the onset and amplification of the type-I MJO convection (e.g., Roundy 2014). When the active (suppressed) phase of the MJO moves from the IO to WP, a positive (negative) PNA pattern is established over the northern Pacific-American-Atlantic sector as documented in previous literature (e.g., Hsu 1996; Mori and Watanabe 2008; Seo and Son 2012; Tseng et al. 2019; Chen 2021). For the type-II (Fig. 7), the upstream and extratropical conditions setup a hostile environment for the MJO. During the onset and development of MJO convection, a robust upper-level westerly (Figs. 7c, d and Fig. 6b) is established by the associated upstream cyclonic anomalies and a quasi-stationary cyclonic gyre over northern Asian-WP sector, which suffocates the type-II MJO within the IO (e.g., Sakaeda and Roundy 2015). The extratropical downstream response is largely influenced by the quasi-stationary cyclonic gyre over the extratropical WP with a negative PNA-like pattern (similar as in Fig. 1f of type-I) over the north Pacific-American-Atlantic sector. For the type-III (Figs. 8, 9, 10), the upstream and extratropical anticyclonic gyres (Figs. 8c, d) establish a robust upper-level easterly (Fig. 6c) over the IO-WP sector. The arrival of a strong east-Asian cold-surge (Figs. 9d, 10d) along with the favorable upper-level condition boosts the rapid development and eastward propagation of the type-III MJO. The induced downstream Kelvin-wave-like response triggers the onset of another MJO event (Figs. 8e, f and Fig. 1c). During the life cycle of the type-III MJO (Figs. 8c, d, e, f), the associated NH extratropical teleconnections evolve from a negative PNA-like pattern (Figs. 8c, d) to a positive PNA-like pattern (Figs. 8e, f) over the northern Pacific-American-Atlantic sector, which result from a combined influence of the MJO convection and the quasi-stationary anticyclone over the northern WP-CP.

A Regional Perspective

The regional and local dynamic and thermodynamic processes associated with the convection of three MJO types over tropical Indo-western Pacific region (from 30^{o}E to 150^{o}W) are carefully examined in Figs. 11, 12, 13, and 14. Under a very favorable large-scale environment (Figs. 2, 5, 6a), the type-I MJO convection (Figs. 11, 12, 13, 14a-d) develops a robust rearward-titling structure of the convergence zone, moisture and EPT along with a robust front (backward) walker cell on the east (west) of the convection. The leading boundary-layer convergence, positive moisture, and convective instability work cooperatively for the development and eastward propagation of the type-I MJO convection. With a hostile large-scale environment (Figs. 3, 7, 6b), the type-II MJO convection (Figs. 11, 12, 13, 14e-h) never develops a robust backward walker cell. A deep front walker cell connects the convection over the IO with the strong dry zone over the WP. Different from the type-I MJO, the drying over the WP is further amplified (Figs. 12f, g) accompanying with the enhanced convection over the IO. The enhanced drying and descending motion over the WP hamper the development of leading boundary-layer convergence and moistening (Figs. 11, 12g) although there is robust leading convective instability (Figs. 13g, h). The convection over the IO

rapidly decays due to the lack of efficient “ventilating” outflows and leading boundary-layer convergence and moistening as well as the intrusion of deep dry anomaly over the WP (Feng et al. 2015; DeMott et al. 2018). Under a moderate favorable environment (Figs. 4, 8, 6c), the type-III MJO convection (Figs. 11, 12, 13, 14i-l) develops rapidly upon the arrival of a strong east-Asian cold-surge. Different from both the type-I and type-II, the type-III MJO has a dominant backward walker cell (Figs. 11j, k, l) instead of a dominant front walker cell (Figs. 11b, c, d and 11f, g), likely due to the lack of a robust deep dry zone preceding the type-III MJO convection (Figs. 12j, k, l). Although no apparent rearward-titling structure is developed, the boundary-layer convergence (Fig. 11l), positive moisture (Fig. 12l) and convective instability (Fig. 13l) over the CP lead the type-III MJO convection to propagate further eastward. For all three MJO types, the associated convection experiences a transition from convective to stratiform regime (Fig. 14) and the persistent positive (Q1-Q2) anomalies at the mature stage testify the important role of radiative heating on sustaining the MJO convection.

A Moisture-budget Perspective

The boundary-layer moisture budget of three MJO types has been assessed in Figs. 15 and 16. The moisture tendency is decomposed into horizontal advection, vertical advection, and moisture sink terms (Fig. 15). The horizontal advection is further decomposed into zonal and meridional advection terms (Fig. 16). For all three MJO types, the positive horizontal advection systematically leads the onset and eastward propagation of the convection (Figs. 15d, i, n), but can’t always manifest as positive boundary-layer moisture tendencies (Figs. 15a, f, k) due to the compromising negative residuals between the vertical advection and moisture sink terms (Figs. 15e, j, o). For the type-I (Figs. 15e, a), the positive moisture tendency consistently leads the onset and eastward propagation of the MJO although the negative residual reduces the amplitude of moisture tendency. The zonal (meridional) advection (Figs. 16a, b) primarily contributes to the onset (eastward propagation). For the type-II (Figs. 15f, j), the positive moisture tendency only leads the onset of the MJO, not the propagation. The negative residual largely cancels the positive horizontal advection on the east of the convection (Figs. 15f, j). Both zonal and meridional advection contribute to the onset (Figs. 16d, e). For the type-III (Figs. 15k, o), positive moisture tendency only leads the eastward propagation of the convection, not the onset. The negative residual largely cancels the positive horizontal advection during the onset stage of the convection (Figs. 15k, o). The zonal advection is the primary contributor to the eastward propagation of the type-III MJO (Fig. 16a).

Synthesizing the results of Fu et al. (2018a) for three boreal-summer MJO types with the findings of present study, it is noticed that the non-propagating type-II MJO has little to do with the so-called MC barrier effect. During boreal summer, we found that the decaying type-II MJO largely results from the lingering convection over the WNP, which enhances the dry zone over the equatorial WP. The latter hampers the formation of robust leading boundary-layer signals (e.g., convergence, moisture, and convective instability), thus confining the type-II convection within the IO. During boreal winter, it is the quasi-stationary cyclonic gyre over the north Asian-Pacific sector and the associated upper-layer westerly suffocates the type-II MJO convection within the IO. The severe dry zone over the WP and lingering

convection over the CP inhibits the formation of leading boundary-layer signals (e.g., convergence, moisture, and convective instability), eventually resulting in the decay of type-II MJO convection within the IO.

Because the longitudinal range of the MC is around 20^{o} and the geomorphology and topography over the MC are constant for all tropical disturbances, it is unclear why the MC halts some MJO events, but not the others. In fact, the MJO-associated convection can well find alternative channels to move through the MC longitudes (e.g., the marginal seas and South China Sea in Wang and Rui 1990). The MJO-associated large-scale circulations have much broader spatial scales than that of the MC. It is the interplay between the large-scale circulations and the convection, involving the tropical-extratropical interactions, top-down and bottom-up influences, play an essential role for the downstream MJO evolutions. The MC barrier problem most likely is a modeling issue originated from misrepresented model processes.

Given that the MJO owns its existence to the coupling between organized multi-scale convection and large-scale Rossby-Kelvin-wave-like circulations in the tropics (e.g., Wang 1988; Majda and Biello 2004; Adames and Wallace 2014; Roundy 2014) and the MJO is primarily fueled by the moisture from underlying ocean, the tropical atmosphere-ocean interactions play important roles on the initiation, intensity, and propagation of the MJO (e.g., Waliser et al. 1999; Fu and Wang 2004). At the same time, many literatures (e.g., Hsu et al. 1990; Hsu 1996; Straub and Kiladis 2002; Lin et al. 2009; Tromeur and Rossow 2010; Sakaeda and Roundy 2015; Abdillah et al. 2021) have documented that the extratropical circulations can well influence the tropical upper-level and low-level environments. Our synergetic glocal analysis further reveals that the diverse behaviors of the MJO can be largely attributed to different tropical-extratropical interactions. For the type-I, the tropical bottom-up processes dominate the tropical and extratropical large-scale responses with the upper-level tropics and extra-tropics behaving collaboratively. For the type-II and type-III, on the other hand, the top-down and extratropical influences are essential. In light that the MJO holds the key for the success of subseasonal-to-seasonal and seamless prediction around the globe, our findings highlight the need to expand the traditional view of the MJO as a tropical mode to a global mode (e.g., Hsu 1996; Donald et al. 2006) in order to accelerate the understanding and modeling of MJO diverse nature and its global influences.

Models are the essential tools used to forecast the MJO and its global impacts. However, it is still unknown to what degree current weather and climate models capture the MJO diversity in nature. Ling et al.(2017) found that latest generation global models failed to reproduce the two favorable onset locations of the MJO in the observations: the western IO and WP, suggesting that present models still have serious problems to reproduce the three MJO types revealed in this study. Xiang et al. (2021) recently revealed that a GFDL model can reproduce some features of MJO diversity and associated teleconnections. As the model skills in forecasting the MJO and its modulations of weather and climate variability largely relies on the model capability in faithfully reproducing the major features of individual MJO events and associated tropical downstream influences and extratropical teleconnections, comprehensive assessments of model simulations of MJO diversity are needed. Multi-model inter-comparisons are recommended to unravel the dominant physical processes misrepresented in current

weather and climate models. The pathways to make improvements should be explored with long-term free runs and short-term initialized runs in the context of atmosphere-only and atmosphere-ocean coupled models.

Declarations

Acknowledgments: This work was jointly supported by the startup fund of Fudan University,

the China National Science Foundation under grant 41875064 and National Key Research Program and Development of China under grant 2017YFC1502302.

References

1. Abdillah, M. R., Y. Kanno, T. Iwasaki, and J. Matsumoto (2021) Cold surge pathways in East Asia and their tropical impacts. J Clim 34, 157-170
2. Adames ÁF, Wallace JM (2014) Three-dimensional structure and evolution of the MJO and its relation to the mean flow. J Atmos Sci 71:2007–2026. https://doi.org/10.1175/jas-d-13-0254.1
3. Barnett T, Graham N, Cane M, et al (1988) On the prediction of the El Niño of 1986-1987. Science 241:192–196
4. Benedict J, Randall DA (2007) Observed characteristics of the MJO relative to maximum rainfall. J Atmos Sci 64:2332–2354. https://doi.org/10.1175/JAS3968.1
5. Bladé I, Hartmann DL (1993) Tropical intraseasonal oscillations in a simple nonlinear model. J Atmos Sci 50:2922–2939
6. Brown TJ, Hall BL (1999) The use of t values in climatological composite analyses. J Clim 12:2941–2945. https://doi.org/10.1175/1520-0442(1999)012<2941:tuotvi>2.0.co;2
7. Chang CP, Chen JM (1992) A statistical study of winter monsoon cold surges over the South China sea and the large-scale equatorial divergence. J Meteorol Soc Jpn 70:157–172. https://doi.org/10.1017/CBO9781107415324.004
8. Chen G (2021) Diversity of the global teleconnections associated with the Madden-Julian oscillation. J Clim 34:397–414. https://doi.org/10.1175/JCLI-D-20-0357.1
9. Chen G, Wang B (2019) Dynamic moisture mode versus moisture mode in MJO dynamics: importance of the wave feedback and boundary layer convergence feedback. Clim Dyn 52:5127–5143. https://doi.org/10.1007/s00382-018-4433-7
10. Chen G, Wang B (2018) Effects of enhanced front walker cell on the eastward propagation of the MJO. J Clim 31:7719–7738. https://doi.org/10.1175/JCLI-D-17-0383.1
11. DeMott CA, Stan C, Randall DA, Branson MD (2014) Intraseasonal variability in coupled GCMs: the roles of ocean feedbacks and model physics. J Clim 27:4970–4995. doi:10.1175/jcli-d-13-00760.1
12. DeMott CA, Wolding BO, Maloney ED, Randall DA (2018) Atmospheric mechanisms for MJO decay over the Maritime Continent. J Geophys Res Atmos 123:5188–

5204. https://doi.org/10.1029/2017JD026979

13. Donald A, Meinke H, Power B, et al (2006) Near-global impact of the Madden-Julian oscillation on rainfall. Geophys Res Lett 33: L09704. doi:10.1029/2005GL025155
14. Duchon CE (1979) Lanczos filtering in one and two dimensions. J Appl Meteorol 18:1016–1022
15. Feng J, Li T, Zhu W (2015) Propagating and non-propagating MJO events over Maritime Continent. J Clim 28:8430–8449. https://doi.org/10.1175/JCLI-D-15-0085.1
16. Fu JX, Wang W, Ren HL, et al (2018a) Three different downstream fates of the boreal-summer MJOs on their passages over the Maritime Continent. Clim Dyn 51:1841–1862. https://doi.org/10.1007/s00382-017-3985-2
17. Fu JX, Wang W, Shinoda T, et al (2017) Toward understanding the diverse impacts of air-sea interactions on MJO Simulations. J Geophys Res Ocea 122:8855–8875. https://doi.org/10.1002/2017JC013187
18. Fu JX, Wang W, Zhu Y, et al (2018b) Impacts of different cumulus schemes on the pathways through which SST provides feedback to the Madden-Julian oscillation. J Clim 31:5559–5579. https://doi.org/10.1175/JCLI-D-17-0432.1
19. Fu X, Wang B (2004) Differences of boreal summer intraseasonal oscillations simulated in an atmosphere-ocean coupled model and an atmosphere-only model. J Clim 17:1263–1271. https://doi.org/10.1175/1520-0442(2004)017<1263:DOBSIO>2.0.CO;2
20. Fu X, Wang W, Lee J-Y, et al (2015) Distinctive roles of air–sea coupling on different MJO events: a new perspective revealed from the DYNAMO/CINDY field campaign. Mon Weather Rev 143:794–812. https://doi.org/10.1175/MWR-D-14-00221.1
21. Gill AE (1980) Some simple solutions for heat-induced tropical circulation. Quart J R Met Soc 106:447–462. https://doi.org/10.1256/smsqj.44904
22. Gloeckler LC, Roundy PE (2013) Modulation of the extratropical circulation by combined activity of the Madden-Julian oscillation and equatorial Rossby waves during boreal winter. Mon Weather Rev 141:1347–1357. https://doi.org/10.1175/MWR-D-12-00179.1
23. Goulet L, Duvel JP (2000) A new approach to detect and characterize intermittent atmospheric oscillations: application to the intraseasonal oscillation. J Atmos Sci 57: 2397–2416
24. Hagos SM, Zhang C, Feng Z, et al (2016) The impact of the diurnal cycle on the propagation of Madden-Julian Oscillation convection across the Maritime Continent. J Adv Model Earth Syst, 8, 1552–1564
25. Harris, L. and Coauthors, 2020: GFDL SHiELD: A unified system for weather-to-seasonal prediction. J Adv Model Earth Syst, 12, e2020MS002223
26. Hendon HH (1988) A simple model of the 40–50-day oscillation. J Atmos Sci 45:569–584
27. Hendon HH, Salby ML (1994) The life cycle of the Madden–Julian Oscillation. J Atmos Sci 51:2225–2237

28. Hersbach H, Bell B, Berrisford P, et al (2020) The ERA5 global reanalysis. Q J R Meteorol Soc 10:15. https://doi.org/10.1002/qj.3803
29. Hersbach H, Rosnay P De, Bell B, et al (2018) Operational global reanalysis: progress, future directions and synergies with NWP. ERA Rep Ser 27:98. https://doi.org/http://dx.doi.org/10.21957/tkic6g3wm
30. Higgins RW, Mo KC (1997) Persistent North Pacific circulation anomalies and the tropical intraseasonal oscillation. J Clim 10:223–244
31. Hirata FE, Webster PJ, Toma VE, 2013: Distinct manifestations of austral summer tropical intra-seasonal oscillations. Geophys Res Lett 40:3337–3341. https://doi.org/10.1002/grl.50632
32. Hong CC, Hsu HH, Tseng WL, et al (2017) Extratropical forcing triggered the 2015 Madden-Julian Oscillation-El Niño event. Scientific Reports 7:46692. https://doi.org/10.1038/srep46692
33. Hoskins BJ (2013) The potential for skill across the range of the seamless weather-climate prediction problem: a stimulus for our science. Q J R Meteorol Soc 139:573–584. https://doi.org/10.1002/qj.1991
34. Hoskins BJ, Ambrizzi T (1993) Rossby wave propagation on a realistic longitudinally varying flow. J Atmos Sci 50:1661–1671. https://doi.org/10.1175/15200469(1993)-050<1661:RWPOAR>2.0.CO;2
35. Hsu HH (1996) Global view of the intraseasonal oscillation during northern winter. J Clim 9:2386–2406
36. Hsu HH, Hoskins BJ, Jin FF (1990) The 1985/86 intraseasonal oscillation and the role of the extratropics. J Atmos Sci 47:823–839
37. Hsu HH, Lee MY (2005) Topographic effects on the eastward propagation and initiation of the Madden-Julian oscillation. J Clim 18:795–809. https://doi.org/10.1175/JCLI-3292.1
38. Hsu PC, Li T (2012) Role of the boundary layer moisture asymmetry in causing the eastward propagation of the Madden-Julian oscillation. J Clim 25:4914–4931
39. Hsu PC, Li T, Murakami H (2014) Moisture asymmetry and MJO eastward propagation in an aquaplanet general circulation model. J Clim 27:8747–8760
40. Hung CS, Sui CH (2018) A diagnostic study of the evolution of the MJO from Indian Ocean to Maritime Continent: Wave dynamics versus advective moistening processes. J Clim 31:4095–4115. https://doi.org/10.1175/JCLI-D-17-0139.1
41. Hung M-P, Lin J-L, Wang W, et al (2013) MJO and convectively coupled equatorial waves simulated by CMIP5 climate models. J Clim 26:6185–6214
42. Inness PM, Slingo JM (2003) Simulation of the Madden-Julian oscillation in a coupled general circulation model. Part I: Comparison with observations and an atmosphere-only GCM. J Clim 16:345–364
43. IPCC (2021) Climate change 2021: the physical science basis: contribution of working group I to the sixth assessment report of the intergovernmental panel on climate change. Cambridge University Press. https://www.ipcc.ch/report/ar6/wg1

44. Jiang XA, Li T (2005) Reinitiation of the boreal summer intraseasonal oscillation in the Tropical Indian Ocean. J Clim 18:3777–3795. https://doi.org/10.1175/JCLI3516.1
45. Jin F, Hoskins BJ (1995) The direct response to tropical heating in a baroclinic atmosphere. J Atmos Sci 52:307–319. https://doi.org/10.1017/CBO9781107415324.004
46. Johnson RH, Ciesielski PE, Ruppert JH, Katsumata M (2015) Sounding-based thermodynamic budgets for DYNAMO. J Atmos Sci 72:598–622. https://doi.org/10.1175/JAS-D-14-0202.1
47. Johnson RH, Rickenbach TM, Rutledge SA, et al (1999) Trimodal characteristics of tropical convection. J Clim 12:2397–2418
48. Kemball-Cook S, Weare BC (2001) The onset of convection in the Madden-Julian Oscillation. J Clim 14:780–793
49. Kerns BW, Chen SS (2016) Large-scale precipitation tracking and the MJO over the Maritime Continent and Indo-Pacific warm pool. J Geophys Res Atmos 121:8755–8776. https://doi.org/10.1002/2015JD024661
50. Kessler WS (2001) EOF representations of the Madden-Julian oscillation and its connection with ENSO. J Clim 14(13):3055–3061
51. Kiladis GN, Dias J, Straub KH, et al (2014) A Comparison of OLR and circulation-based indices for tracking the MJO. Mon Weather Rev 142:1697–1715. https://doi.org/10.1175/MWR-D-13-00301.1
52. Kiladis GN, Straub KH, Haertel PT (2005) Zonal and vertical structure of the Madden-Julian oscillation. J Atmos Sci 62:2790–2809. https://doi.org/10.1175/JAS3520.1
53. Kim DH, Kug J-S, Sobel AH (2014) Propagating versus non-propagating Madden-Julian oscillation events. J Clim 27:111–125. https://doi.org/10.1175/JCLI-D-13-00084.1
54. Kiranmayi L, Maloney ED (2011) Intraseasonal moist static energy budget in reanalysis data. J Geophys Res Atmos 116: D21117. https://doi.org/10.1029/2011JD016031
55. Knutson TR, Weickmann KM (1987) 30–60 day atmospheric oscillations: composite life cycles of convection and circulation anomalies. Mon Weather Rev 115:1407–1436. https://doi.org/10.1175/1520-0493(1987)115<1407:DAOCLC>2.0.CO;2
56. Kosaka Y, Nakamura H (2006) Structure and dynamics of the summertime Pacific-Japan teleconnection pattern. Q J R Meteorol Soc 132:2009–2030
57. Krishnamurti TN, Jayakumur PK, Sheng J, et al (1985) Divergent circulations on the 30 to 50 day time scale. J Atmos Sci 42:364–375. https://doi.org/10.1175/15200469(1985)042<0364:DCOTTD>2.0.CO;2
58. Lau K-M, Chan PH (1985) Aspects of the 40-50 day oscillation during the northern winter as inferred from outgoing longwave radiation. Mon Weather Rev 113: 1889-1909
59. Lau K-M, Peng L (1987) Origin of low-frequency (intraseasonal) oscillations in the tropical atmosphere. Part I: basic theory. J Atmos Sci 44:950–972. https://doi.org/10.1175/1520-0469(1987)044<0950:oolfoi>2.0.co;2

60. Lau, K. M., and D. E. Waliser (2012): Intraseasonal variability in the Atmosphere-Ocean climate system (second version). Springer, Praxis publishing, Chichester, UK, p613
61. Lavender SL, Matthews AJ (2009) Response of the West African monsoon to the Madden-Julian oscillation. J Clim 22:4097–4116. https://doi.org/10.1175/2009JCLI2773.1
62. Lee RW, Woolnough SJ, Charlton-Perez AJ, Vitart F (2019) ENSO modulation of MJO teleconnections to the North Atlantic and Europe. Geophys Res Lett 46:13535–13545. https://doi.org/10.1029/2019GL084683
63. Li C, Jia X, Ling J, et al (2009) Sensitivity of MJO simulations to diabatic heating profiles. Clim Dyn 32:167–187. https://doi.org/10.1007/s00382-008-0455-x
64. Liebmann B, Hartmann DL (1984) An observational study of tropical-midlatitude interaction on intraseasonal time scales during winter. J Atmos Sci 41:3333–3350
65. Liebmann B, Smith CA (1996) Description of a complete (interpolated) outgoing longwave radiation dataset. Bull Am Meteorol Soc 77:1275–1277
66. Ling J, Li C, Zhou W, Jia X (2014) To begin or not to begin? A case study on the MJO initiation problem. Theor Appl Climatol 115:231–241
67. Ling J, Zhang C, Bechtold P (2013) Large-scale distinctions between MJO and non-MJO convective initiation over the tropical Indian Ocean. J Atmos Sci 70:2696–2712. https://doi.org/10.1175/JAS-D-13-029.1
68. Ling J, Zhang C, Joyce R, et al (2019) Possible role of the diurnal cycle in land convection in the barrier effect on the MJO by the Maritime Continent. Geophys Res Lett 46:3001–3011. https://doi.org/10.1029/2019GL081962
69. Ling J, Zhang C, Wang S, Li C (2017) A new interpretation of the ability of global models to simulate the MJO. Geophys Res Lett 44:5798–5806
70. Lin H, Brunet G, Derome J (2009) An observed connection between the North Atlantic oscillation and the Madden-Julian oscillation. J Clim 22:364–380. https://doi.org/10.1175/2008JCLI2515.1
71. Lin X, Johnson RH (1996) Heating, moistening, and rainfall over the western Pacific Warm Pool during TOGA COARE. J Atmos Sci 53:3367–3383. https://doi.org/10.1175/1520-0469(1996)053<3367:HMAROT>2.0.CO;2
72. Li T, Tam F, Fu X, et al (2008) Causes of the intraseasonal SST variability in the tropical Indian Ocean. Atmos Ocea Sci Lett 1:18–23
73. Lorenc AC (1984) The evolution of planetary-scale 200 mb divergent flow during the FGGE year. Q J R Meteorol Soc 110:427–441. https://doi.org/10.1002/qj.49711046408
74. Madden RA, Julian PR (1971) Detection of a 40–50 day oscillation in the zonal wind in the tropical Pacific. J Atmos Sci 28:702–708
75. Madden RA, Julian PR (1972) Description of global-scale circulation cells in the tropics with a 40–50 day period. J Atmos Sci 29:1109–1123

76. Majda A, Biello J (2004) A multiscale model for tropical intraseasonal oscillations. Proc Natl Acad Sci USA 101:4736–4741. https://doi.org/10.1073/pnas.0401034101
77. Maloney ED, Hartmann DL (2000) Modulation of hurricane activity in the Gulf of Mexico by the Madden- Julian oscillation. Science 287:2002–2004
78. Maloney ED, Sobel AH, Hannah WM (2010) Intraseasonal variability in an aquaplanet general circulation model. J Adv Model Earth Syst 2:1-24. https://doi.org/10.3894/james.2010.2.5
79. Matthews AJ (2000) Propagation mechanisms for the Madden-Julian oscillation. Q J R Meteorol Soc 126:2637–2651. https://doi.org/10.1007/BF01215203
80. Matthews AJ, Hoskins BJ, Masutani M (2004) The global response to tropical heating in the Madden-Julian Oscillation during the northern winter. Q J R Meteorol Soc 130:1991–2011. https://doi.org/10.1256/qj.02.123
81. Matthews AJ, Kiladis GN (1999) The tropical-extratropical interaction between high-frequency transients and the Madden-Julian oscillation. Mon Weather Rev 127:661–677. https://doi.org/10.1175/1520-0493(1999)127<0661:TTEIBH>2.0.CO;2
82. Mei S, Li T, Chen W (2015) Three-type MJO initiation processes over the Western Equatorial Indian Ocean. Adv Atmos Sci 32:1208–1216. https://doi.org/10.1007/s00376-015-4201-0
83. Moore R, Martius O, Spengler T (2010) The modulation of the subtropical and extratropical atmosphere in the pacific basin in response to the Madden-Julian Oscillation. Mon Weather Rev 138:2761–2779. https://doi.org/10.1175/2010MWR3194.1
84. Mori M, Watanabe M (2008) The growth and triggering mechanisms of the PNA: a MJO-PNA coherence. J Meteorol Soc Jpn 86:213–236. https://doi.org/10.2151/jmsj.86.213
85. Murakami T (1988) Intraseasonal atmospheric teleconnection patterns during the northern hemisphere winter. J Clim 1:117–131
86. Oh JH, Kim KY, Lim GH (2012) Impact of MJO on the diurnal cycle of rainfall over the western Maritime Continent in the austral summer. Clim Dyn 38:1167–1180. https://doi.org/10.1007/s00382-011-1237-4
87. Pang B, Lu R, Ling J (2018) Impact of cold surges on the Madden-Julian oscillation propagation over the Maritime Continent. Atmos Sci Lett 19(10): e854
88. Qi Hu, Randall DA (1994) Low-frequency oscillations in radiative-convective systems. J Atmos Sci 51:1089–1099. https://doi.org/10.1175/15200469(1994)051<1089:lfoirc>-2.0.co;2
89. Raymond DJ, Torres DJ (1998) Fundamental moist modes of the equatorial troposphere. J Atmos Sci 55:1771-1790
90. Ray P, Li T (2013) Relative roles of circumnavigating waves and extratropics on the MJO and its relationship with the mean state. J Atmos Sci 70:876–893. https://doi.org/10.1175/JAS-D-12-0153.1
91. Ray P, Zhang C (2010) A case study of the mechanics of extratropical influence on the initiation of the Madden-Julian oscillation. J Atmos Sci 67:515–528. https://doi.org/10.1175/2009JAS3059.1

92. Ray P, Zhang C, Dudhia J, Chen SS (2009) A numerical case study on the initiation of the Madden-Julian oscillation. J Atmos Sci 66:310–331
93. Roundy PE (2012) Observed structure of convectively coupled waves as a function of equivalent depth: Kelvin waves and the Madden-Julian oscillation. J Atmos Sci 69:2097–2106. https://doi.org/10.1175/JAS-D-12-03.1
94. Roundy PE (2014) Some aspects of western hemisphere circulation and the Madden-Julian oscillation. J Atmos Sci 71:2027–2039. https://doi.org/10.1175/JAS-D-13-0210.1
95. Rui H, Wang B (1990) Development characteristics and dynamic structure of tropical intraseasonal convection anomalies. J Atmos Sci 47(3):357–379
96. Sakaeda N, Roundy PE (2015) The development of upper-tropospheric wind over the Western Hemisphere in association with MJO convective initiation. J Atmos Sci 72:3138–3160. https://doi.org/10.1175/JAS-D-14-0293.1
97. Sardeshmukh PD, Hoskins BJ (1988) The generation of global rotational flow by steady idealized tropical divergence. J Atmos Sci 45:1228–1251
98. Seo KH, Kim KY (2003) Propagation and initiation mechanism of the Madden-Julian oscillation. J Geophys Res 108:4384. https://doi.org/10.1029/2002jd002876
99. Seo KH, Son SW (2012) The global atmospheric circulation response to tropical diabatic heating associated with the Madden-Julian oscillation during northern winter. J Atmos Sci 69:79–96. https://doi.org/10.1175/2011JAS3686.1
100. Seo KH, Wang W (2010) The Madden-Julian oscillation simulated in the NCEP climate forecast system model: The importance of stratiform heating. J Clim 23:4770–4793. https://doi.org/10.1175/2010JCLI2983.1
101. Shinoda T, Hendon HH, Glick J (1998) Intraseasonal variability of surface fluxes and sea surface temperature in the tropical western Pacific and Indian Oceans. J Clim 11: 1685-1702. https://doi.org/10.1175/1520-0442(1998)011<1685:IVOSFA>2.0.CO;2
102. Sobel AH, Maloney ED, Bellon G, Frierson DM (2010) Surface fluxes and tropical intraseasonal variability: a reassessment. J Adv Model Earth Syst 2: 2. https://doi.org/10.3894/james.2010.2.2
103. Takaya K, Nakamura H (2001) A formulation of a phase-independent wave-activity flux for stationary and migratory quasigeostrophic eddies on a zonally varying basic flow. J Atmos Sci 58:608–627
104. Tan H, Ray P, Barrett BS, et al (2020) Role of topography on the MJO in the maritime continent: a numerical case study. Clim Dyn 55:295–314
105. Trenberth KE (1991) Climate diagnostics from global analyses: conservation of mass in ECMWF analyses. J Clim 4:707–722
106. Tromeur E, Rossow WB (2010) Interaction of tropical deep convection with the large-scale circulation in the MJO. J Clim 23(7):1837–1853. doi:10.1175/2009JCLI3240.1
107. Tseng KC, Maloney E, Barnes E (2019) The consistency of MJO teleconnection patterns: An explanation using linear Rossby wave theory. J Clim 32:531–548. https://doi.org/10.1175/JCLI-D-

18-0211.1

108. Waliser DE, Lau KM, Kim JH (1999) The influence of coupled sea surface temperatures on the Madden-Julian oscillation: a model perturbation experiment. J Atmos Sci 56:333–358. https://doi.org/10.1175/1520-0469(1999)056<0333:TIOCSS>2.0.CO;2
109. Wang B (1988) Dynamics of tropical low-frequency waves: an analysis of the moist Kelvin wave. J Atmos Sci 45:2051–2065
110. Wang B, Chen G, Liu F (2019) Diversity of the Madden-Julian oscillation. Sci Adv 5: eaax0220. https://doi.org/10.1126/sciadv.aax0220
111. Wang B, Rui H (1990) Synoptic climatology of transient tropical intraseasonal convection anomalies: 1975-1985. Meteorol Atmos Phys 44:43–61
112. Wang L, Li T, Nasuno T (2018) Impact of Rossby and Kelvin wave components on MJO eastward propagation. J Clim 31:6913–6931. https://doi.org/10.1175/JCLI-D-17-0749.1
113. Wang WQ, Schlesinger ME (1999) The dependence on convection parameterization of the tropical intraseasonal oscillation simulated by the UIUC 11-layer atmospheric GCM. J Clim 12: 1423-1457
114. Wolding BO, Maloney ED (2015) Objective diagnostics and the Madden–Julian Oscillation. Part II: Application to moist static energy and moisture budgets. J Clim 28:7786–7808. https://doi.org/10.1175/JCLI-D-14-00689.1
115. Wu CH, Hsu HH (2009) Topographic influence on the MJO in the Maritime Continent. J Clim 22:5433–5448. https://doi.org/10.1175/2009JCLI2825.1
116. Wu J, Zhang P, Li L, et al (2020) Representation and predictability of the East Asia-Pacific teleconnection in the Beijing Climate Center and UK Met Office subseasonal prediction systems. J Meteorol Re 34:941–964
117. Xiang, B. Q., and Coauthors, 2021: S2S prediction in GFDL SPEAR: MJO Diversity and Teleconnections. Bull Am Meteorol Soc, In press.
118. Yanai M, Esbensen S, Chu J-H (1973) Determination of bulk properties of tropical cloud clusters from large-scale heat and moisture budgets. J Atmos Sci 30:611–627
119. Zhang C (2005) The Madden-Julian Oscillation. Rev Geophys 43: RG2003
120. Zhang C (2013) Madden–Julian Oscillation: bridging weather and climate. Bull Am Meteorol Soc 94:1849–1870. https://doi.org/10.1175/bams-d-12-00026.1
121. Zhang C, Adames ÁF, Khouider B, Wang B, Yang D (2020) Four theories of the Madden-Julian Oscillation. Rev Geophys 58: e2019RG000685
122. Zhao C, Li T, Zhou T (2013) Precursor signals and processes associated with MJO initiation over the tropical Indian Ocean. J Clim 26:291–307. https://doi.org/10.1175/JCLI-D-12-00113.1
123. Zhu B, Wang B (1993) The 30–60 day convection seesaw between the tropical Indian and western Pacific Oceans. J Atmos Sci 50:184–199

Figures

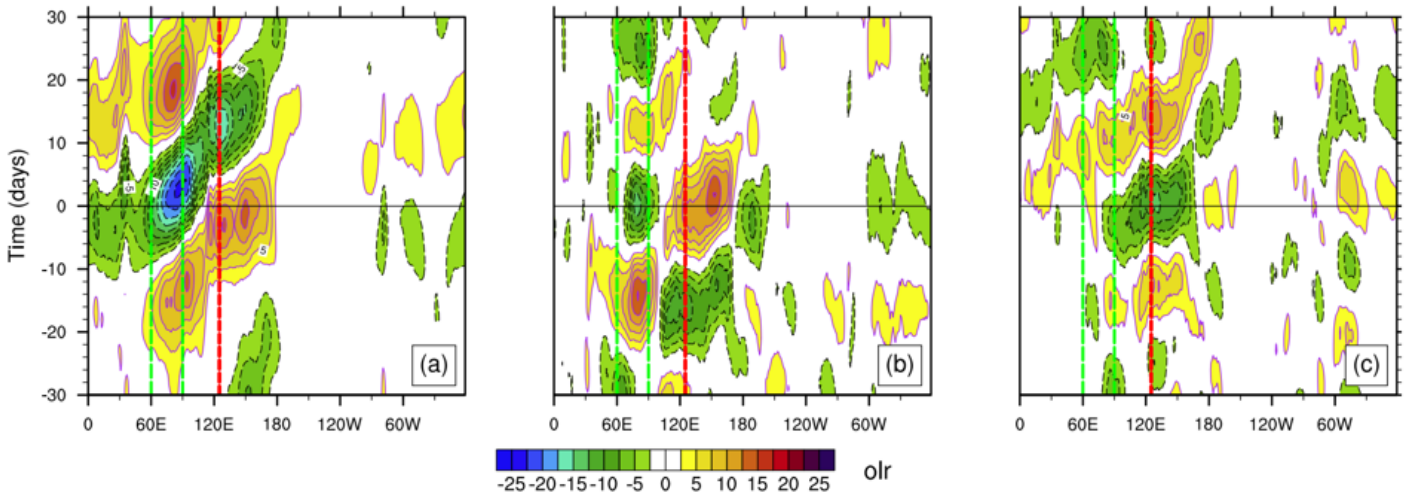

Figure 1

Composite time-longitude sections of OLR anomalies (CI: 2.5 Wm-2) averaged between 10°S-10°N, with the longitudes spanning from 0°E to 0°W. For type-I (a), type-II (b), and type-III (c), from day -30 to +30. Only the regions statistically significant above 5% level are plotted. The dash (solid) lines represent negative (positive) OLR anomalies. The two green vertical lines highlight the IO, and the red one is the 125°E longitude as the threshold to distinguish type-I and type-II MJO events.

Figure 2

Composite horizontal spatial-temporal evolutions of OLR (shading, Wm-2), 200-hPa velocity potential (VP200) (contour, CI: 4×〖10〗^5 m^2 s^(-2)) and the associated divergent wind (vector, m s-1) anomalies, from day -25 to +20, for type-I MJO. The red solid contour represents the positive VP200 (convergence) and the blue dash contour represents the negative VP200 (divergence). The OLR, VP200 and divergent wind vectors are shown for those statistically significant above 5% level. The two boxes mark the locations of two MJO activity centers: the red one represents the EIO (15°S-15°N, 70°E-100°E) and the green one represents the MC-WP (15°S-15°N, 120°E-180°E).

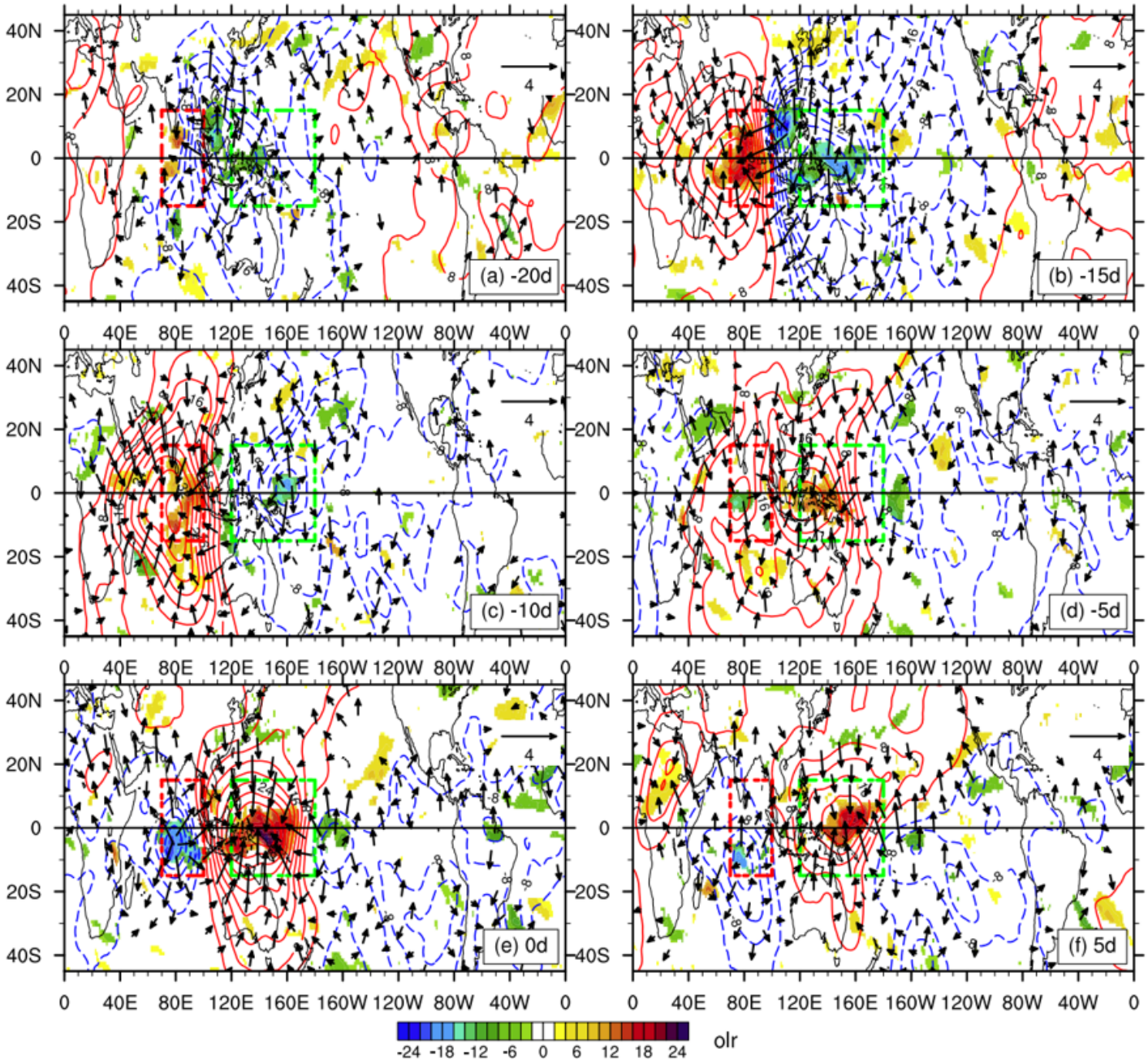

Figure 3

As in Fig. 2, but for type-II MJO, from day -20 to +5.

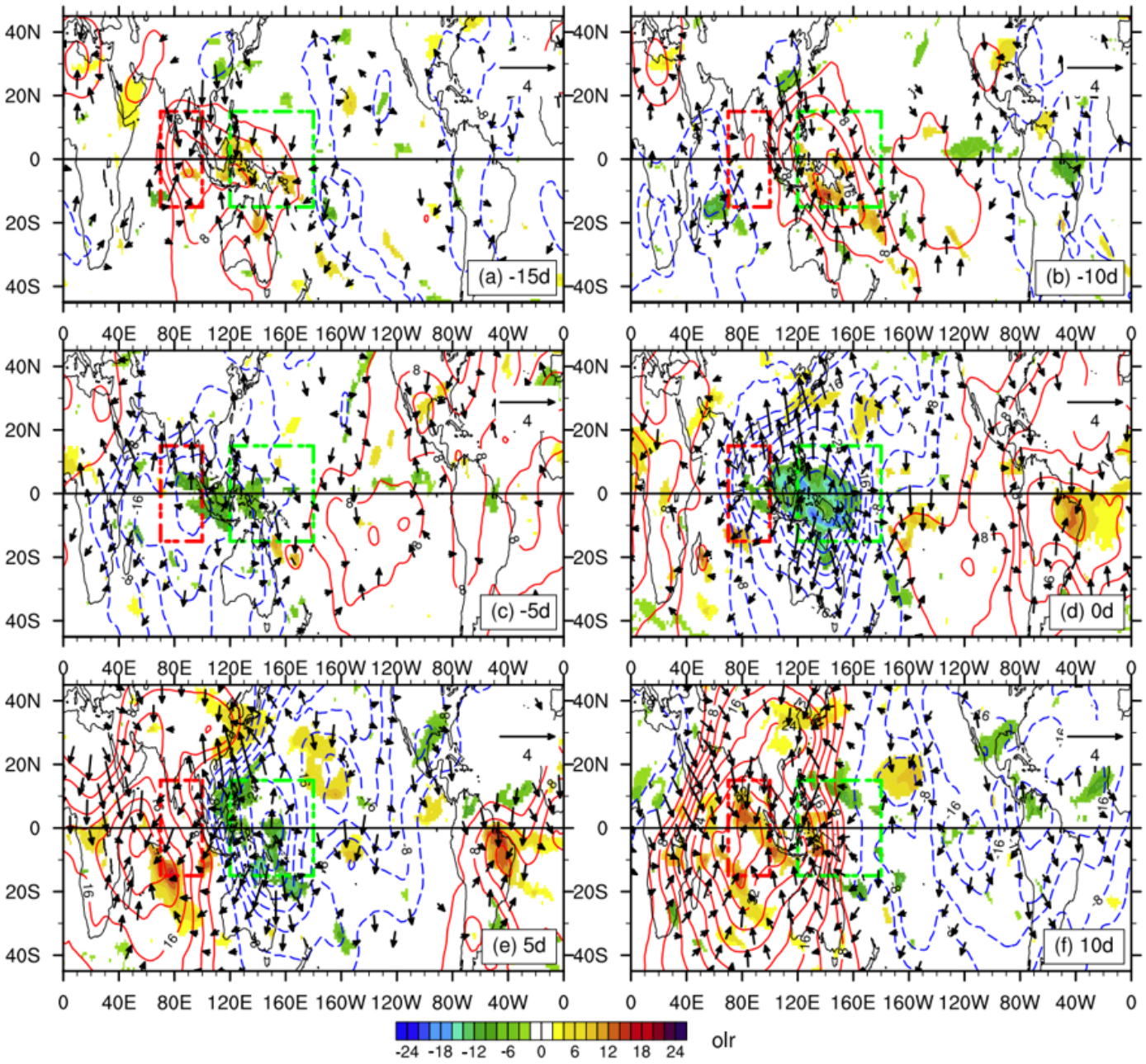

Figure 4

As in Fig. 2, but for type-III MJO, from day -15 to +10.

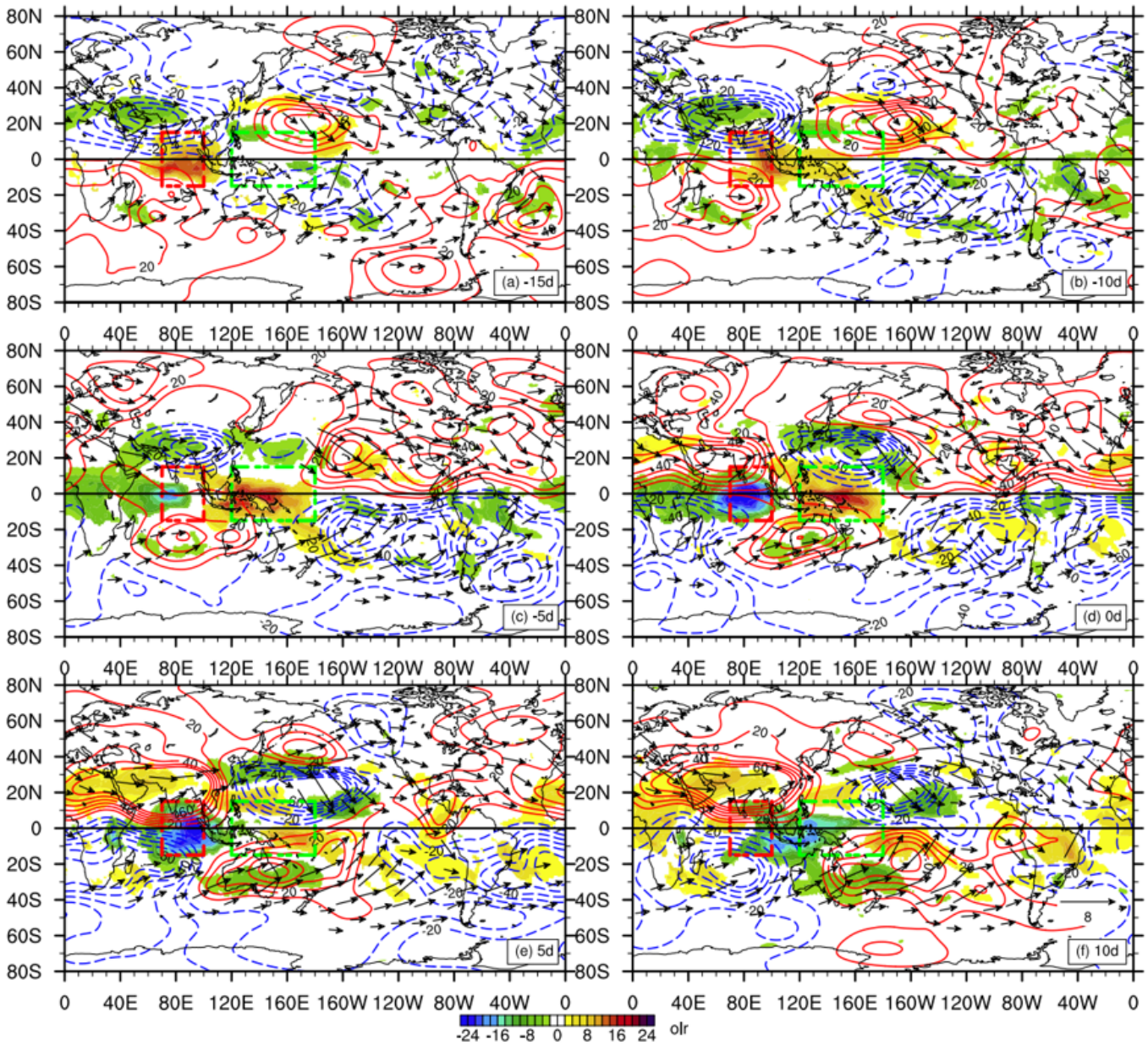

Figure 5

Composite horizontal spatial-temporal evolutions of OLR (shading, Wm-2), 200-hPa stream function (SF200) (contour, CI: 2×⟦10⟧^6 m^2 s^(-1)) and the associated wave activity flux (m2s-2) anomalies, from day -15 to +10, for type-I MJO. The red solid contour represents the positive SF200 (anticyclonic anomaly over NH and cyclonic anomaly over SH) and the blue dash contour represents the negative SF200 (cyclonic anomaly over NH and anticyclonic anomaly over SH). The OLR, SF200 and wave activity flux vectors are shown for those statistically significant above 5% level. The two boxes mark the locations of two MJO activity centers: the red one represents the EIO (15°S-15°N, 70°E-100°E) and the green one represents the MC-WP (15°S-15°N, 120°E-180°E).

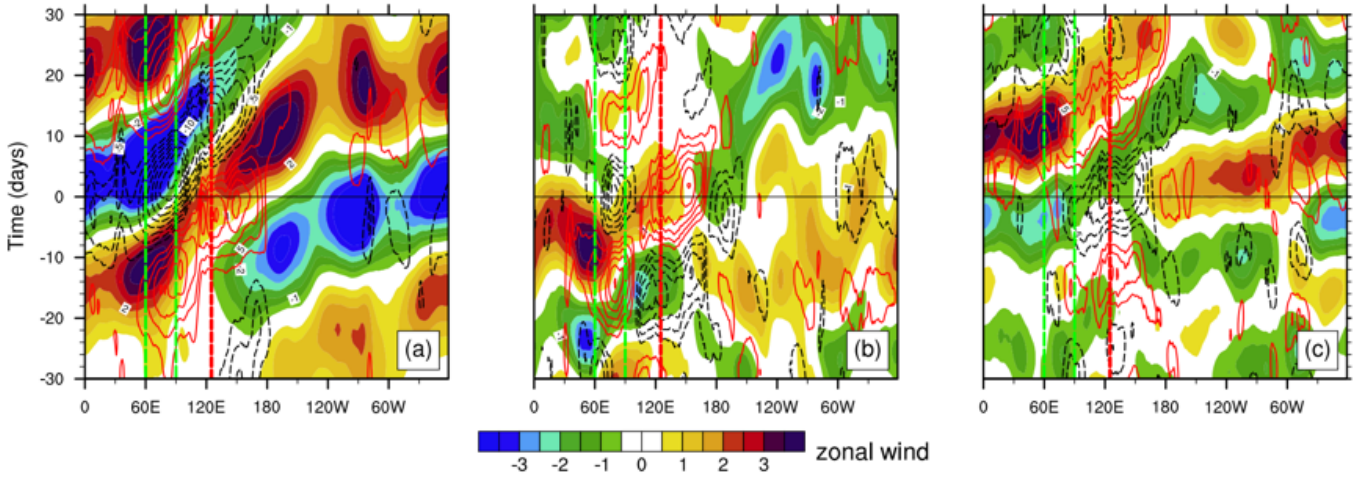

Figure 6

Composite global time-longitude Hovmo¨ller diagrams of 200-hPa zonal wind (shading, ms-1) and OLR (contour, CI: 2.5 Wm-2) anomalies averaged between 10°S-10°N. For type-I (a), type-II (b), and type-III (c), from day -30 to +30. Only the regions statistically significant above 5% level are plotted. The dash (solid) lines represent negative (positive) OLR anomalies. The two green vertical lines highlight the IO, and the red one is the 125°E longitude as the threshold to distinguish type-I and type-II MJO events.

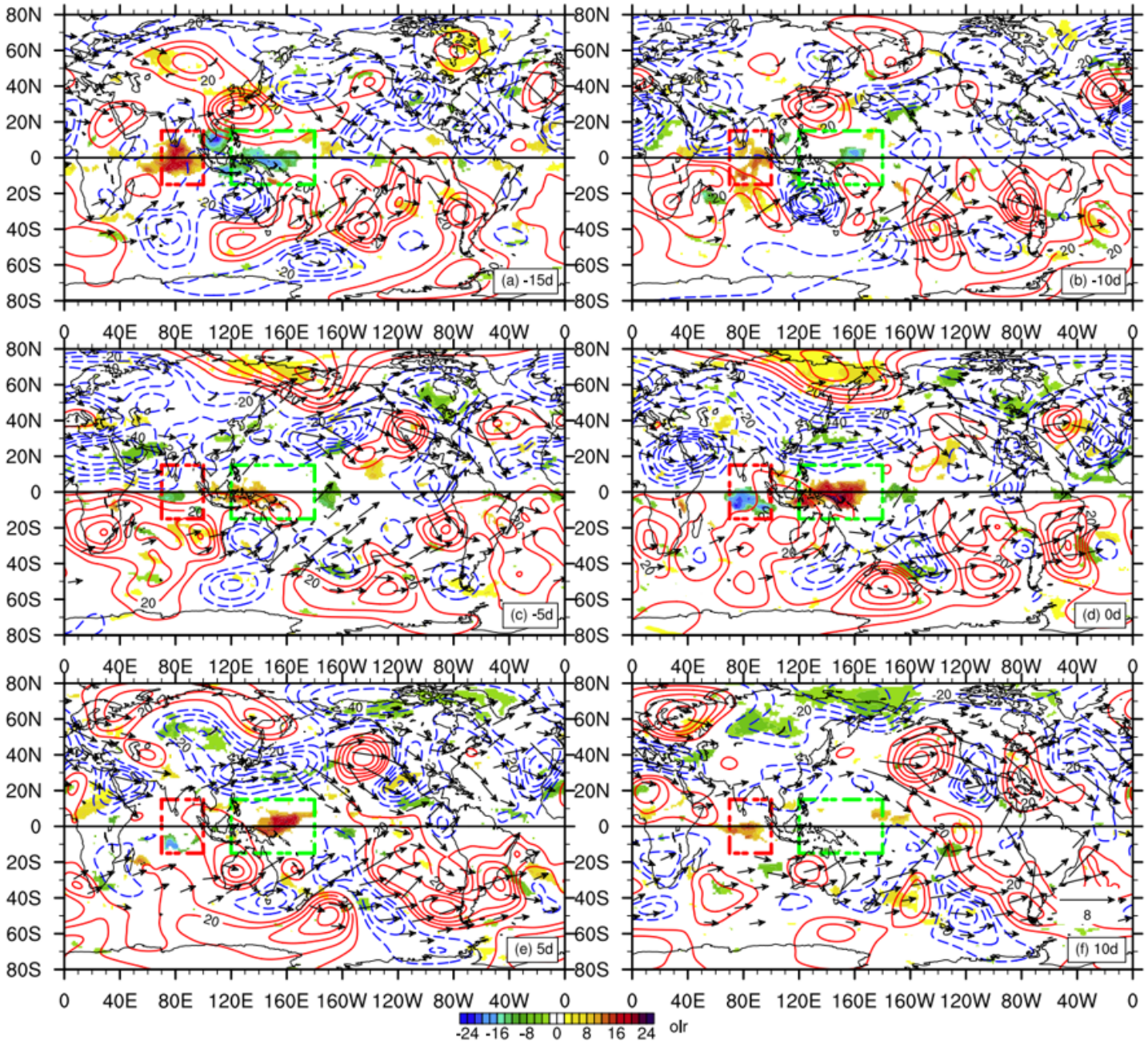

Figure 7

As in Fig. 5, but for type-II MJO.

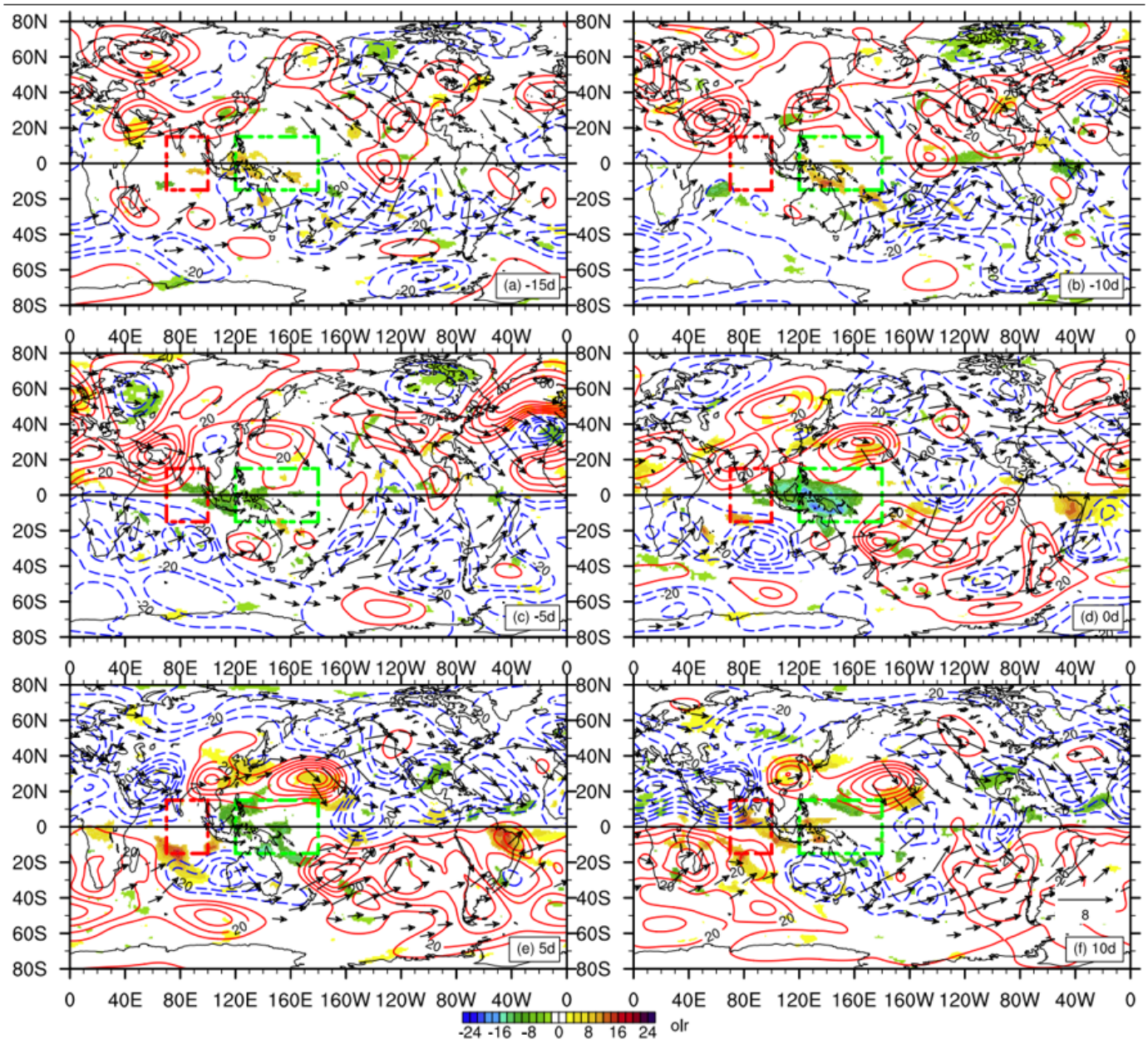

Figure 8

As in Fig. 5, but for type-III MJO.

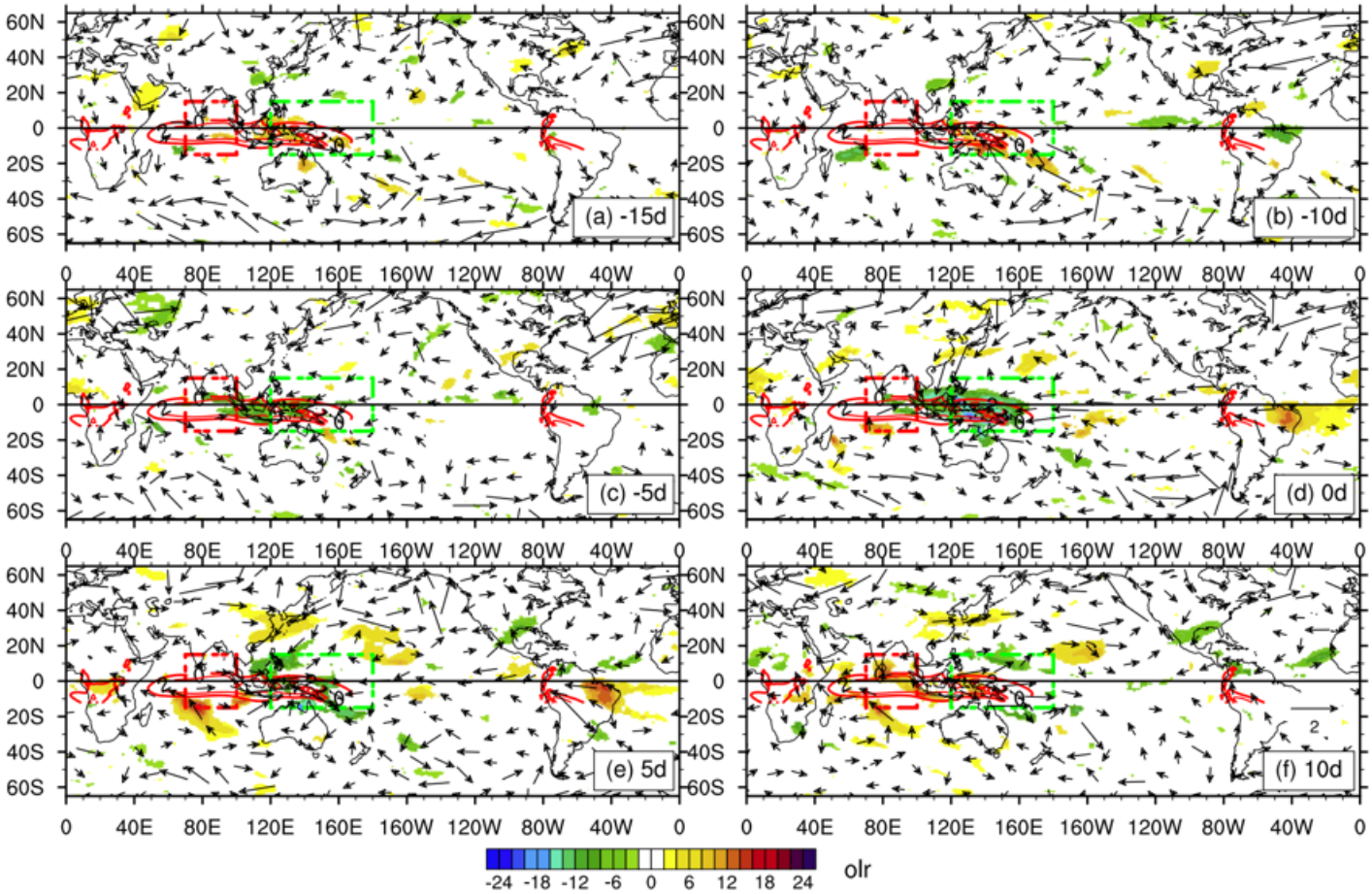

Figure 9

Composite horizontal spatial-temporal evolutions of OLR (shading, Wm-2), 850-hPa wind (vector ms-1) anomalies, from day -15 to +10, for type-III MJO. The red thick contour represents the boreal winter climatological westerly wind averaged between the 10°S-10°N. The OLR and wind vectors are shown for those statistically significant above 5% level. The two boxes mark the locations of two MJO activity centers: the red one represents the EIO (15°S-15°N, 70°E-100°E) and the green one represents the MC-WP (15°S-15°N, 120°E-180°).

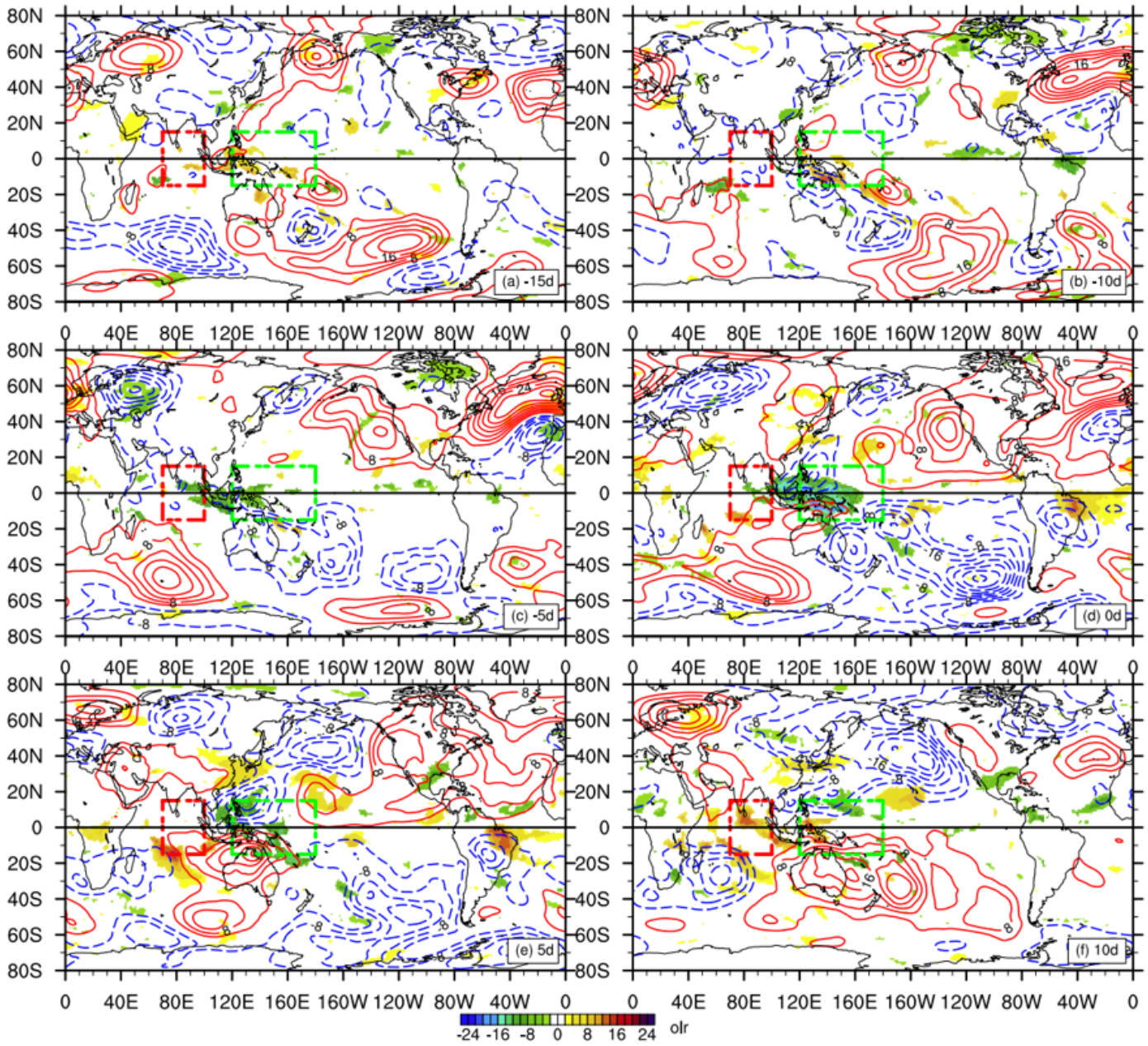

Figure 10

Composite horizontal spatial-temporal evolutions of OLR (shading, Wm-2), 850-hPa stream function (SF850) (contour, CI: 2×⟦10⟧^6 m^2 s^(-1)), from day -15 to +10, for type-III MJO. The red solid contour represents the positive SF850 (anticyclonic anomaly over NH and cyclonic anomaly over SH) and the blue dash contour represents the negative SF850 (cyclonic anomaly over NH and anticyclonic anomaly over SH). The OLR, SF850 are shown for those statistically significant above 5% level. The two boxes mark the locations of two MJO activity centers: the red one represents the EIO (15°S-15°N, 70°E-100°E) and the green one represents the MC-WP (15°S-15°N, 120°E-180°E).

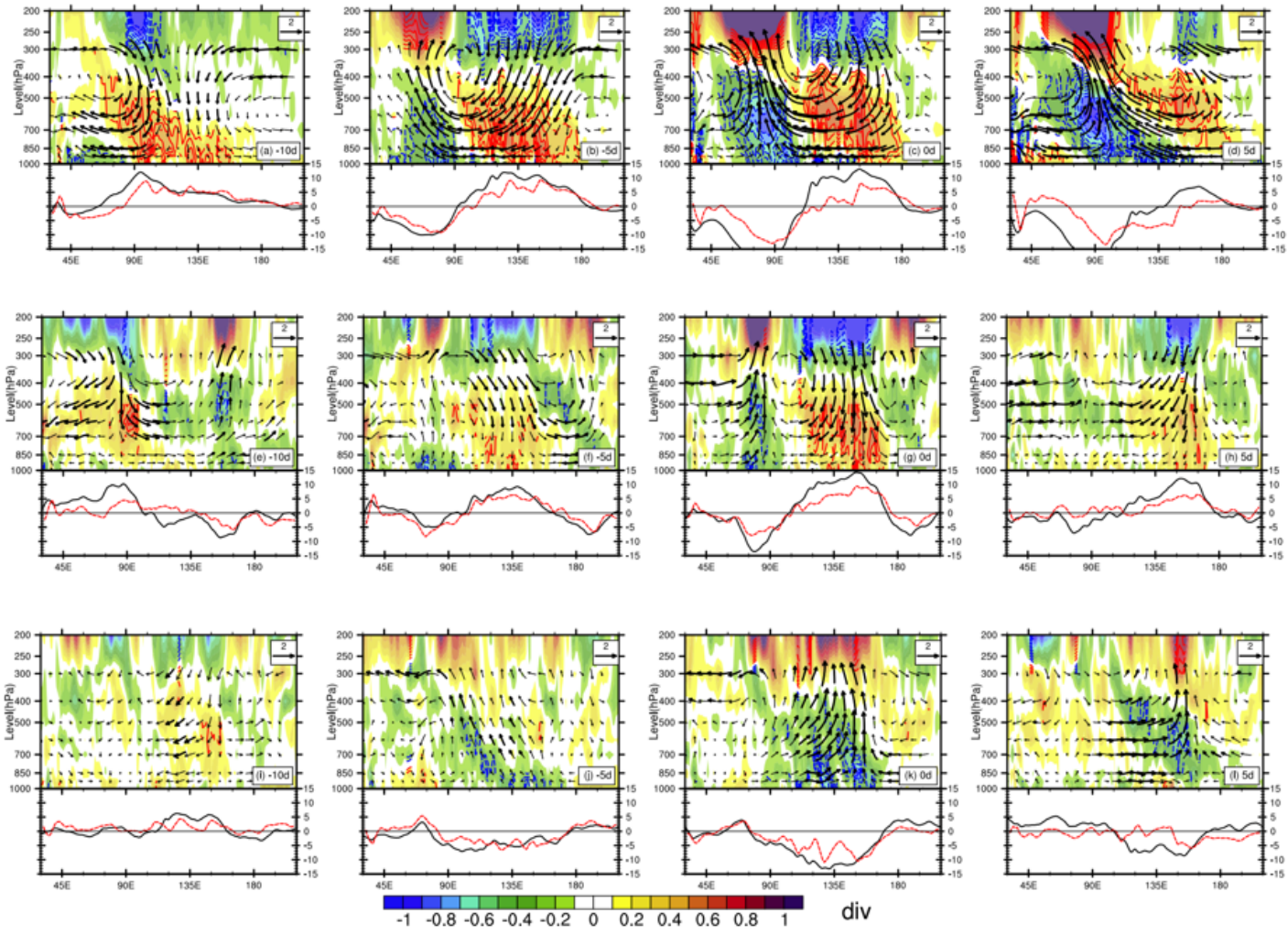

Figure 11

Composite vertical structures of horizontal divergence anomalies (shading, 1×⟦10⟧^(-6) s^(-1)) and the anomalous wind (vectors, representing the zonal and vertical wind; The vertical wind anomalies are multiplied by a factor of -100) overlay the boundary-layer integrated (1000-700-hPa) horizontal divergence (red dash line, multiplied by a factor of 20) and OLR (black line, Wm-2) anomalies averaged between 10°S and 10°N at day -10, -5, 0 and +5 for MJO type-I (top panel: a, b, c, d), type-II (middle panel: e, f, g, h), and type-III (bottom-panel: i, j, k, l). For the convergence fields, values statistically significant above 5% are shown by contours, the red one represents positive anomalies (convergence) and the blue one represents negative anomalies (divergence).

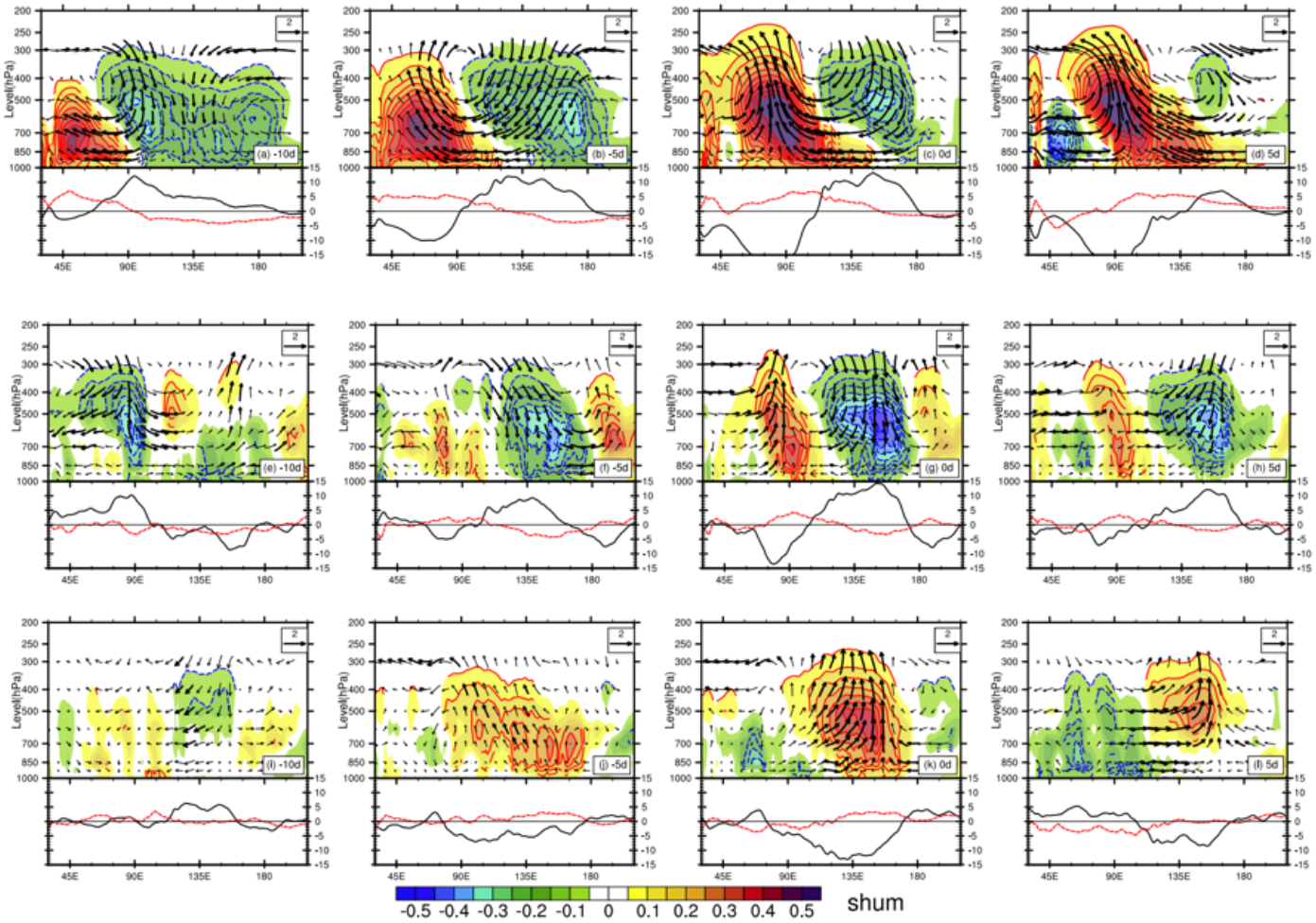

Figure 12

As Fig. 11, but for the specific humidity (gkg-1) overlaying the OLR (black line), the boundary-layer integrated (1000-700-hPa) specific humidity (multiplied by a factor of 20).

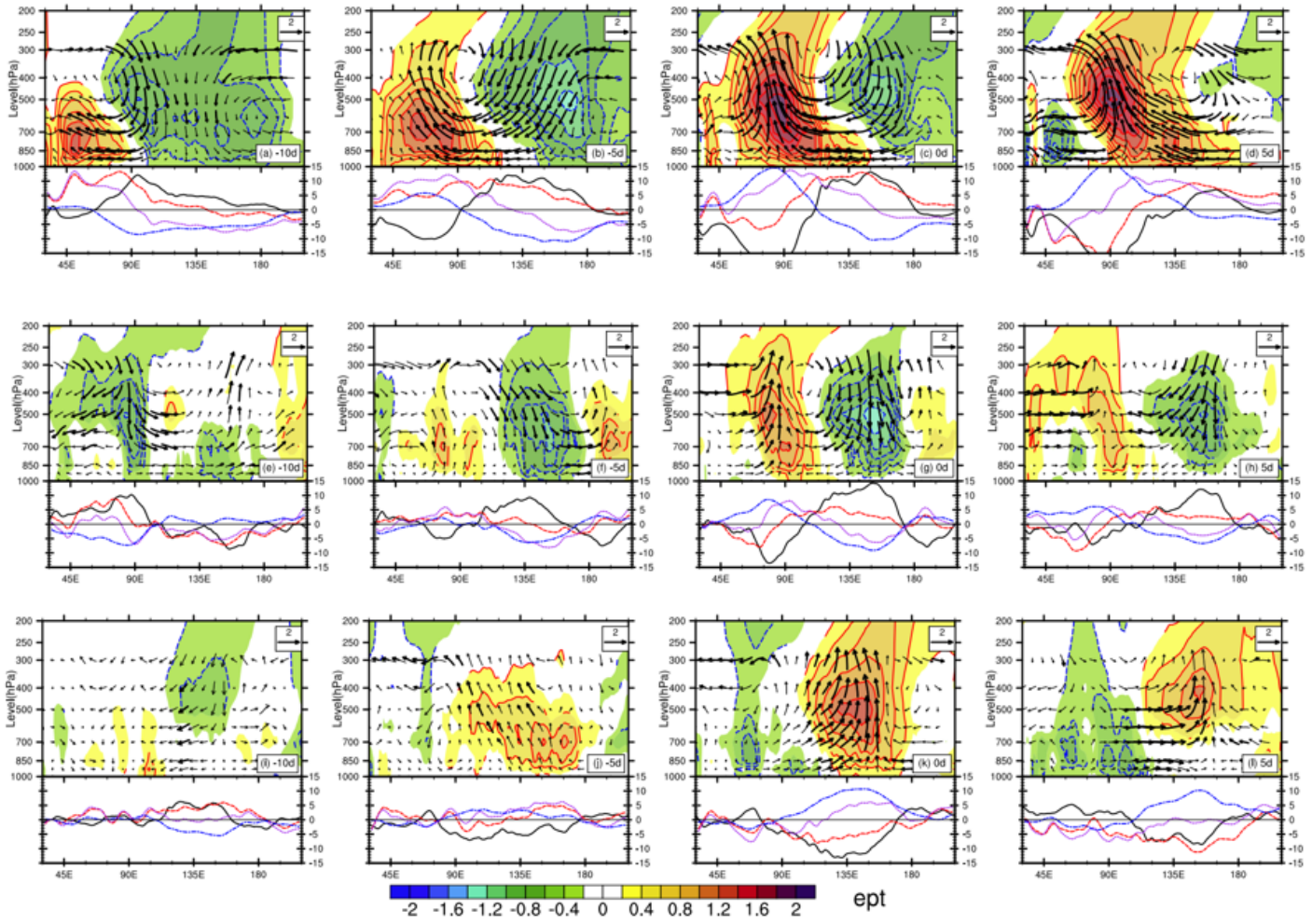

Figure 13

As Fig. 11, but for the equivalent potential temperature (K) overlaying the OLR (black line), the convective instability index measured by the equivalent potential temperature (EPT) difference between 850-hPa and 400-hPa (red dash line: EPT 850 minus EPT 400; purple line: 850-hPa EPT; blue line: 400-hPa EPT, all of them are multiplied by a factor of 10).

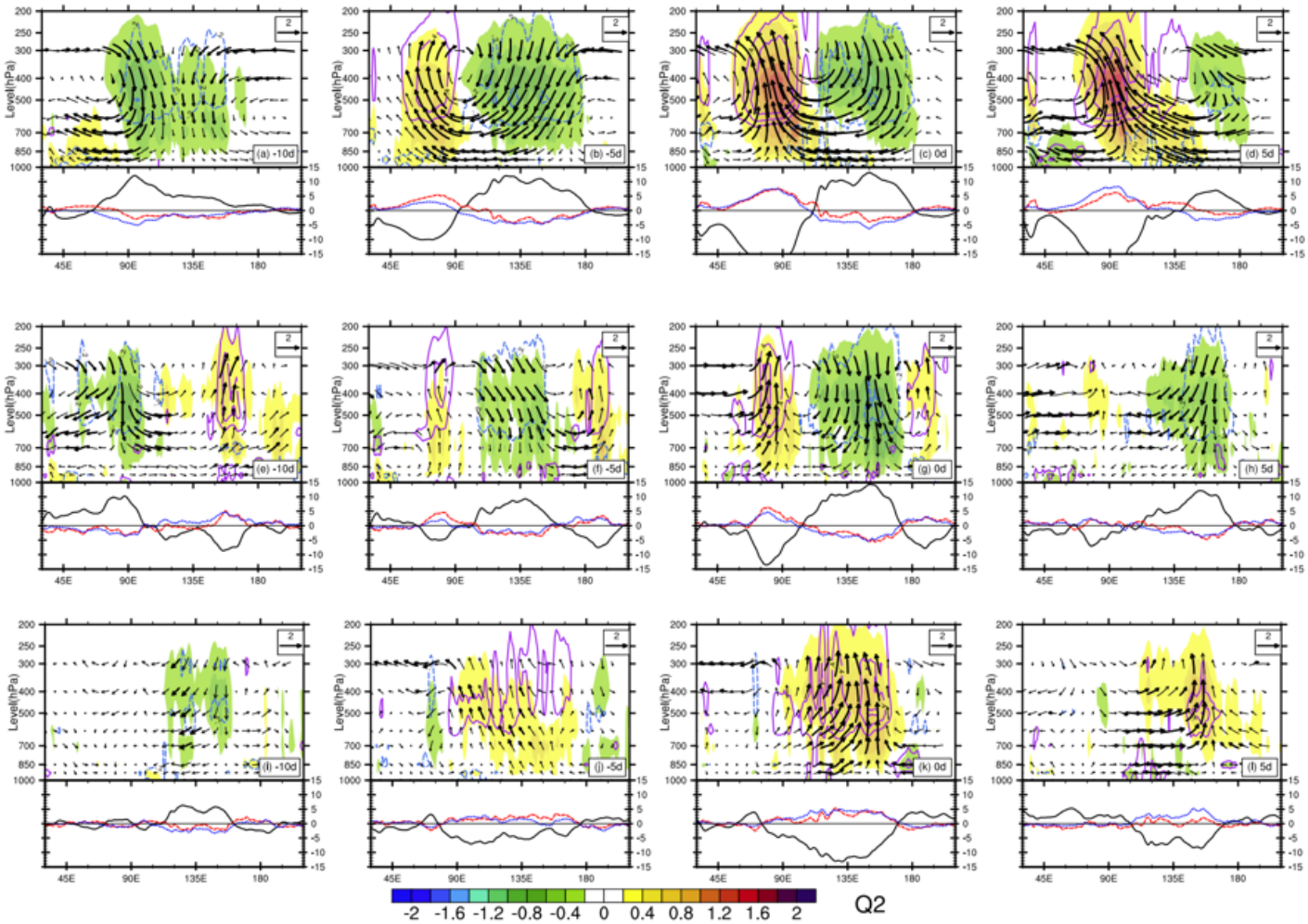

Figure 14

As Fig. 11, but for the apparent moisture sink term (shading, Q2, Kday-1), and Q1-Q2 (contour, CI: 0.2 Kday-1 representing the radiative heating and eddy vertical flux convergence) overlaying the OLR (black line), Q1-Q2 (red dash line, multiplied by a factor of 10), and the Q2 (blue dash line, multiplied by a factor of 10) at 300-hPa. Only those statistically significant above 5% level are shown.

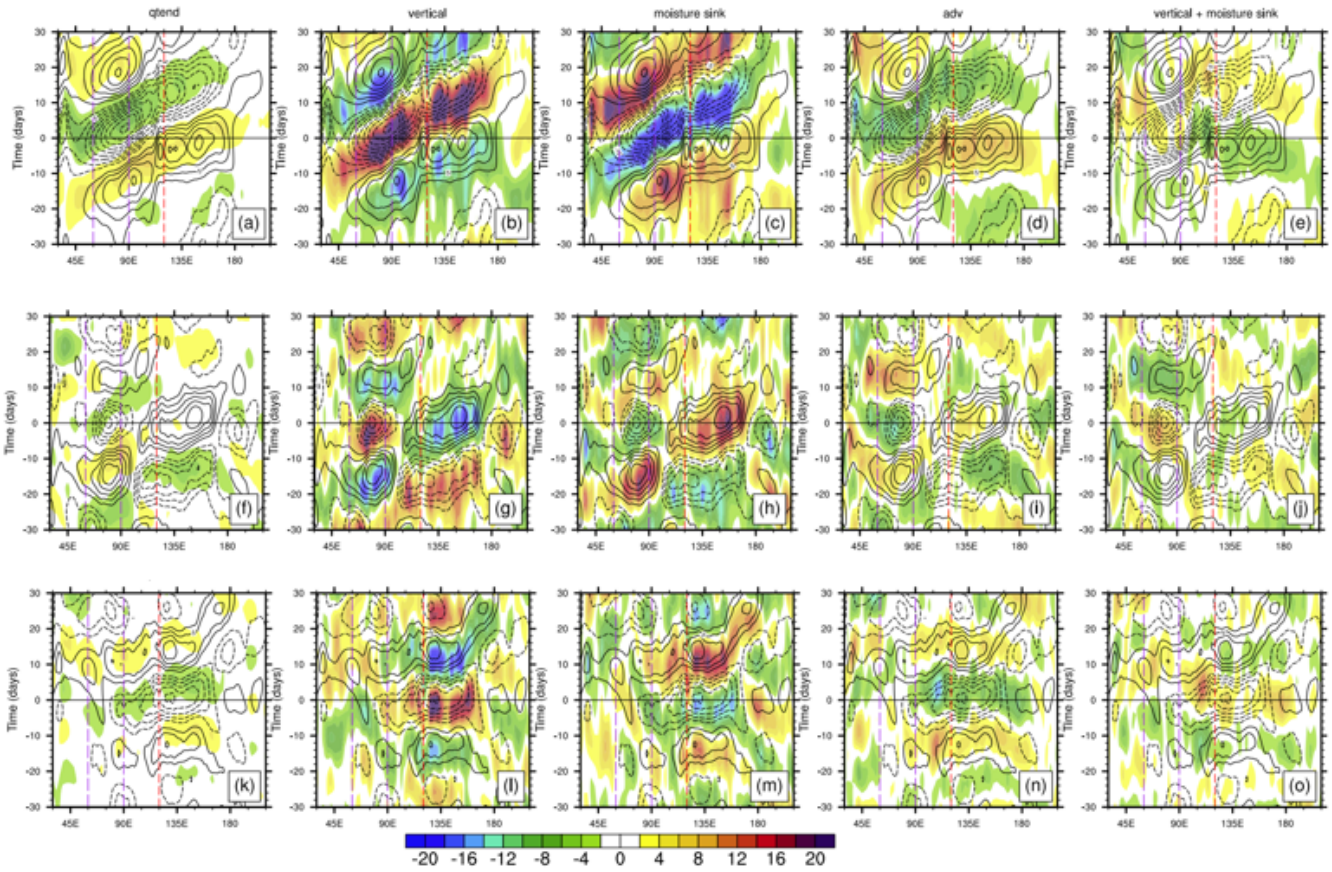

Figure 15

Composite time-longitude sections of 1000-700-hPa integrated moisture budget terms (shading: 1×10-7 gkg-1s-1) and OLR anomalies (contour, CI: 2.5 Wm-2), (a, f, k) tendency, (b, g, l) vertical advection, (c, h, m) horizontal advection, (d, i, n) moisture sink, (e, j, o) vertical term adds moisture sink term, from day -30 to +30. Only the regions statistically significant above 5% level are plotted. The dash (solid) lines represent negative (positive) OLR anomalies. The two green vertical lines highlight the IO, and the red one is the 125°E longitude as the threshold to distinguish type-I and type-II MJO events. For three MJO types: type-I, type-II, and type-III (top, middle and bottom).

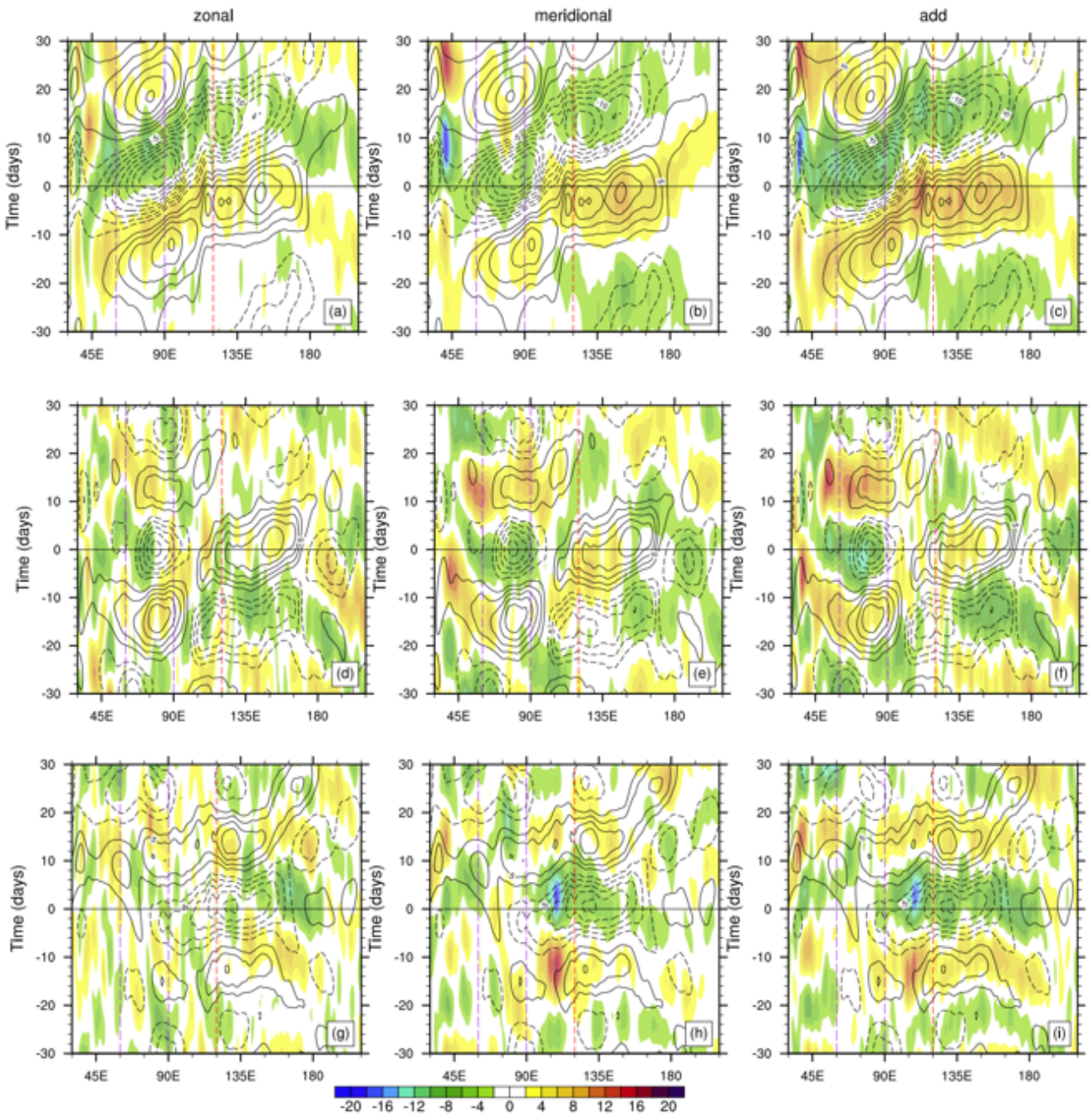

Figure 16

Composite time-longitude evolutions of 1000-700-hPa integrated moisture budget terms (shading: 1×10-7 gkg-1s-1) and OLR anomalies (contour, CI: 2.5 Wm-2): (a, d, g) zonal advection, (b, e, h) meridional advection, and (c, f, i) horizontal (add) advection from day -30 to +30 for type-I (top), type-II (middle), and type-III (bottom). Only the regions statistically significant above 5% level are plotted. The dash (solid) lines represent negative (positive) OLR anomalies. The two purple vertical lines highlight the IO region, and the red one is the 125°E longitude.

Supplementary Files

This is a list of supplementary files associated with this preprint. Click to download.

- supplementaryrevised.docx